NASA/TM-20250003695

A Novel Laser-Processed Condensing Heat Exchanger for Space Systems

Tyler Hatch
Glenn Research Center, Cleveland, Ohio

Jennifer Ferguson
University of Louisville, Louisville, Kentucky

Craig Zuhlke
University of Nebraska–Lincoln, Lincoln, Nebraska

John Sanders
Edare, LLC, Lebanon, New Hampshire

December 2025

NASA STI Program Report Series

Since its founding, NASA has been dedicated to the advancement of aeronautics and space science. The NASA scientific and technical information (STI) program plays a key part in helping NASA maintain this important role.

The NASA STI program operates under the auspices of the Agency Chief Information Officer. It collects, organizes, provides for archiving, and disseminates NASA's STI. The NASA STI program provides access to the NTRS Registered and its public interface, the NASA Technical Reports Server, thus providing one of the largest collections of aeronautical and space science STI in the world. Results are published in both non-NASA channels and by NASA in the NASA STI Report Series, which includes the following report types:

- TECHNICAL PUBLICATION.
  Reports of completed research or a major significant phase of research that present the results of NASA programs and include extensive data or theoretical analysis. Includes compilations of significant scientific and technical data and information deemed to be of continuing reference value. NASA counterpart of peer-reviewed formal professional papers but has less stringent limitations on manuscript length and extent of graphic presentations.

- TECHNICAL MEMORANDUM.
  Scientific and technical findings that are preliminary or of specialized interest, e.g., quick release reports, working papers, and bibliographies that contain minimal annotation. Does not contain extensive analysis.

- CONTRACTOR REPORT.
  Scientific and technical findings by NASA-sponsored contractors and grantees.

- CONFERENCE PUBLICATION.
  Collected papers from scientific and technical conferences, symposia, seminars, or other meetings sponsored or cosponsored by NASA.

- SPECIAL PUBLICATION.
  Scientific, technical, or historical information from NASA programs, projects, and missions, often concerned with subjects having substantial public interest.

- TECHNICAL TRANSLATION.
  English-language translations of foreign scientific and technical material pertinent to NASA's mission.

Specialized services also include organizing and publishing research results, distributing specialized research announcements and feeds, providing information desk and personal search support, and enabling data exchange services.

For more information about the NASA STI program, see the following:

- Access the NASA STI program home page at http://www.sti.nasa.gov

NASA/TM-20250003695

A Novel Laser-Processed Condensing Heat Exchanger for Space Systems

Tyler Hatch
Glenn Research Center, Cleveland, Ohio

Jennifer Ferguson
University of Louisville, Louisville, Kentucky

Craig Zuhlke
University of Nebraska–Lincoln, Lincoln, Nebraska

John Sanders
Edare, LLC, Lebanon, New Hampshire

National Aeronautics and
Space Administration

Glenn Research Center
Cleveland, Ohio 44135

December 2025

Acknowledgments

The authors would like to thank the NASA Polaris Program, specifically J.J. Edelmann, for providing funding for this effort and providing guidance to the team throughout the project. Additionally, we would like to acknowledge NASA Contract 80NSSC22P0096 for allowing both Creare and Edare to support this effort. Dr. Mike Izeson from Creare provided guidance with the numerical model, and John Sanders led the advanced manufacturing and electroplating efforts with Edare and also provided mentorship to the team. We would also like to acknowledge NASA Contract 80NSSC22P0130, which facilitated the UNL work. Dr. Craig Zuhlke, Dr. Jeff Shield, Garrett Beard, Juveriya Parmar, and Suchit Sarin were all instrumental to the success of this project. Various NASA personnel also contributed to this effort. The NASA GRC team beyond the PI included Cody Farinacci, Dr. Ezra McNichols, Kyle Monaghan, and Jennifer Ferguson. The NASA JSC team included Scott Hansen, Jon-Michael Tucker, Dr. Sarah Wallace, and Christian Mena. Finally, we would like to thank the U.S. Army Space and Missile Defense Command Technical Center and the University of Alabama-Huntsville for use of the Pharos femtosecond laser system in the Pulsed Laser Lab, specifically Dr. Anthony Valenzuela for his guidance.

Level of Review: This material has been technically reviewed by technical management.

This report is available in electronic form at https://www.sti.nasa.gov/ and https://ntrs.nasa.gov/

NASA STI Program/Mail Stop 050
NASA Langley Research Center
Hampton, VA 23681-2199

A Novel Laser-Processed Condensing Heat Exchanger for Space Systems

Tyler Hatch
National Aeronautics and Space Administration
Glenn Research Center
Cleveland, Ohio 44135

Jennifer Ferguson
University of Louisville
Louisville, Kentucky 40208

Craig Zuhlke
University of Nebraska–Lincoln
Lincoln, Nebraska 68588

John Sanders
Edare, LLC
Lebanon, New Hampshire 03766

Summary

Condensing heat exchangers (CHXs) are commonly used for spacecraft life support as part of the overall environmental control subsystem. They allow water from humid air to be collected and circulated back into the water reclamation unit on orbit. To optimize such a system, limited allowable pressure drops and a specified vapor recuperation rate must be achievable. Traditionally, numerical models rely on established heat transfer and pressure drop correlations. This project investigated the addition of dimples to the heat exchanger surface for improved convective heat transfer, but this meant that the flat-plate correlations initially used in the laminar model needed to be updated to a k-ω turbulence model. Additionally, manufacturing advantages of electroplating the components together were investigated and documented through microscopy analyses. The wetting properties of the system were achieved through a laser-processing treatment via dual-pulse femtosecond laser surface processing, which also provides microbial tolerance to the hardware. The aftereffects of laser processing on the electroplated system were also investigated. This project's effort toward reducing overall manufacturing time and yielding enhanced performance over current state-of-the-art space CHX systems has applications for long-duration spaceflight, such as a future Mars mission.

1.0 Introduction

The International Space Station (ISS) relies on numerous advanced systems to support long-duration space exploration, one of which is the condensing heat exchanger (CHX). The CHX is designed to reduce cabin humidity and regulate temperature by extracting moisture from the air. However, its current design depends on a coating that prematurely loses its hydrophilic properties, leading to water carryover into the cabin and frequent refurbishments. The 2020 NASA Technology Taxonomy roadmap, a tiered Agency plan of action, identifies this issue as a Tier 1 Gap (Gap 06-50), meaning a solution to the premature decomposition of wetting properties is high on the priority list (Ref. 1).

Recent advancements in manufacturing have demonstrated the viability of electroplating for CHX development. Despite its novelty for use with CHX materials, the electroplating process described here has the potential to reduce overall manufacturing challenges, cutting production time by 18 months and saving over $1 million in costs (Ref. 2). Prior work on a stainless steel and silver packet in a CHX unit has been performed, using femtosecond laser surface processing (FLSP) to modify the surface properties to enhance wetting behaviors without relying on coating applications (Ref. 3). NASA's Laser Processed Condensing Heat Exchanger (LP-CHX) project was established to further explore the manufacturing process, seeking to significantly reduce lead time and improve overall cost. A preexisting pressure drop thermal model was reviewed and updated in tandem with the potential design changes to create a more accurate picture of the anticipated performance and account for scaling up from breadboard-size models to production size.

This report details the initial efforts to model the heat transfer properties of a new LP-CHX using an updated thermal-fluid model. It provides a summary of the validity of electroplating for this purpose, microscopy data for the laser-treated plates, and results of microbial testing on this surface. The report also discusses design changes driven by testing data, such as the addition of dimples to enhance performance. Initially absent from heat transfer calculations due to limited data, the dimple pattern was later incorporated into an updated simulation, run in parallel with a new computational fluid dynamics (CFD) model to validate the findings.

The LP-CHX project was developed to address current issues with CHX systems in space. Current CHX technology utilizes hydrophilic coating to gather condensate and control microbial growth in conjunction with a monthly dry-out. ISS "slurper" bars and a water separator are used to draw condensate off the CHX, delivering it to the Water Processor Assembly (WPA). However, there are three main problems with the current technology:

- The contamination turns the hydrophilic surfaces hydrophobic, leading to water carryover and significantly limiting condensate reclamation. As a result, CHXs must be uninstalled and refurbished on a regular basis, costing significant crew time and resources.
- Microbial growth in the CHX can impede its performance over time and could pose biological threats to the crew. The current ISS CHX coating utilizes an antimicrobial component in its coating to mitigate microbe growth and must be dried out monthly to prevent biofilm formation. This leads to additional logistics tracking within Mission Control and may not eliminate microbial growth as desired.
- Existing coatings may react with airborne contaminants, which can lead to downstream impacts on the WPA. A chemical reaction between airborne contaminants and the hydrophilic coating is thought to potentially produce dimethylsilanediol (DMSD), a chemical that degrades filters in the WPA. Currently, WPA filters can remove compounds, but the filters are degraded at an accelerated rate, needing to be replaced every year rather than every other year as originally planned.

This project addressed Tier 1 Gap 06-50 by expanding on recent efforts for ground-based development of a novel silver-plated heat exchanger (HX) that solves all three problems of current CHXs. This technology is currently at a Technology Readiness Level (TRL) of 4. With use of the LP-CHX, the requirement for a chemical coating is eliminated, the monthly dry-outs may be excluded due to significant microbial growth mitigation, and the possibility of DMSD production is very limited given that a chemical coating is not used.

Throughout this report, units of measure are given as originally reported. Nomenclature is provided in Appendix A, and additional figures are provided in Appendix B.

2.0 Project Scope

This technology meets performance targets of long life, chemically inert condensing surfaces, microgravity-compatible systems, and microbial growth resistance. It fulfills mass, volume, and thermal performance requirements as well as other considerations, such as sparing and redundancy. In May 2020, this technology was highly favored during a CHX technology down-select held with NASA's Habitation Systems, Advanced Explorations Systems, and key members of the Environmental Control and Life Support Systems (ECLSS) Systems Capability Leadership Team (SCLS). Unfortunately, the manufacturing process used for the original LP-CHX design was time consuming and cost prohibitive. The process required numerous manual laser welds and nested coolant channels made with stainless steel and silver condensing surface packets, and it used a low-power laser that would require approximately 19 months to laser-process condensing surfaces.

An alternative manufacturing process using electroplating has been identified that would reduce these manufacturing complexities. Specifically, this process would allow silver to be deposited directly onto stainless steel rather than enveloping a stainless steel channel with thermal interface material and a separate silver sheet or packet. Using this process would reduce the number of laser welds by half and eliminate the need for nested packets. It is estimated that this new design would decrease manufacturing costs and time by over $1 million and 4 months. Following successful efforts to identify and integrate a more powerful laser, the laser processing time has been decreased by more than 16 to 18 months. With investments in this technology, the LP-CHX can now be feasibly manufactured.

3.0 Work Performed at NASA Glenn Research Center

The CHX modeling effort by the NASA Glenn Research Center utilized the theoretical packet design in a thermal fluid model, updating the design as needed after receiving data collection from laboratory testing done at the NASA Johnson Space Center. The goal was to investigate key performance indicators (KPIs) for the scaled model, validated with simulation, to determine correlations and tuning for a new, expanded computational model for the full system as integrated into the ISS Common Cabin Air Assembly. This full-scale modeling data was used as a metric for performance of the entire system as the manufacturing complexities of electroplating, laser processing of dimples, and other aspects were investigated to determine the most feasible path to full-scale construction (Ref. 4).

3.1 Condensing Heat Exchanger Overview

The CHX system consists of a stack of fluid-air HX plates arranged to form a cassette, as illustrated in Figure 1. To enable water condensation out of the humid air, the plates are cooled via a cooling loop circulating along the upper section. Air flows through narrow channels between the fluid-air heat plates, where it condenses and is collected for transport back into the water reclamation system. Increasing the height of these channels for more airflow can reduce the pressure drop in the system but also results in a lower heat transfer efficiency and decreased condensation rate. The optimal air channel height was determined to be 1.0668 mm (0.042 in.) using optimization modeling.

Additionally, a dimpled surface was incorporated on the air-facing side of the fluid-air HX, as depicted in Figure 2. These dimples, which measure 0.508 mm (0.02 in.) in convex height, spaced 5.7404 mm (0.226 in.) apart in both the x and y directions, disrupt airflow to promote circulation and enhance condensation. Slices of the dimpled surfaces with their temperature condition ranges can be seen in Figure 3 to Figure 5.

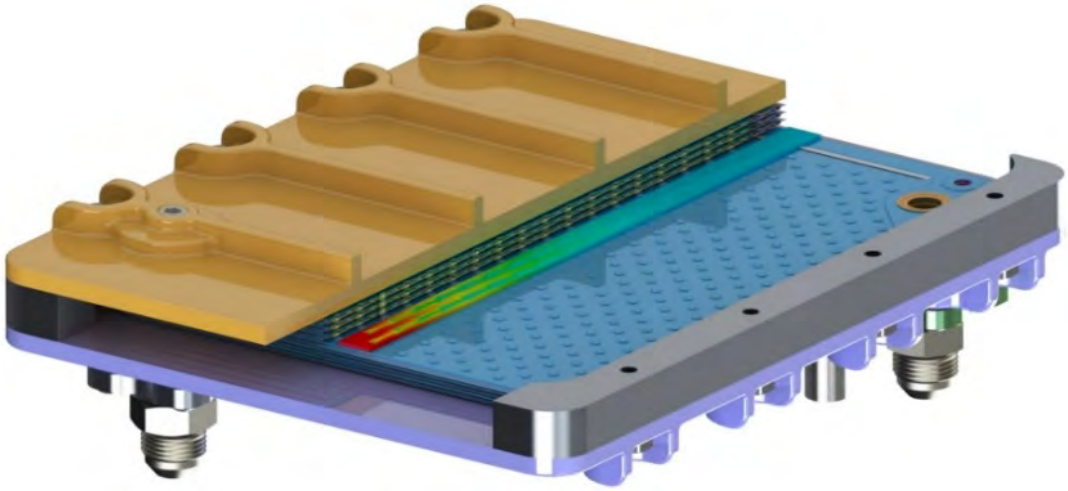

Figure 1.—Cutaway rendering of LP-CHX with CFD domain superimposed (Ref. 2).

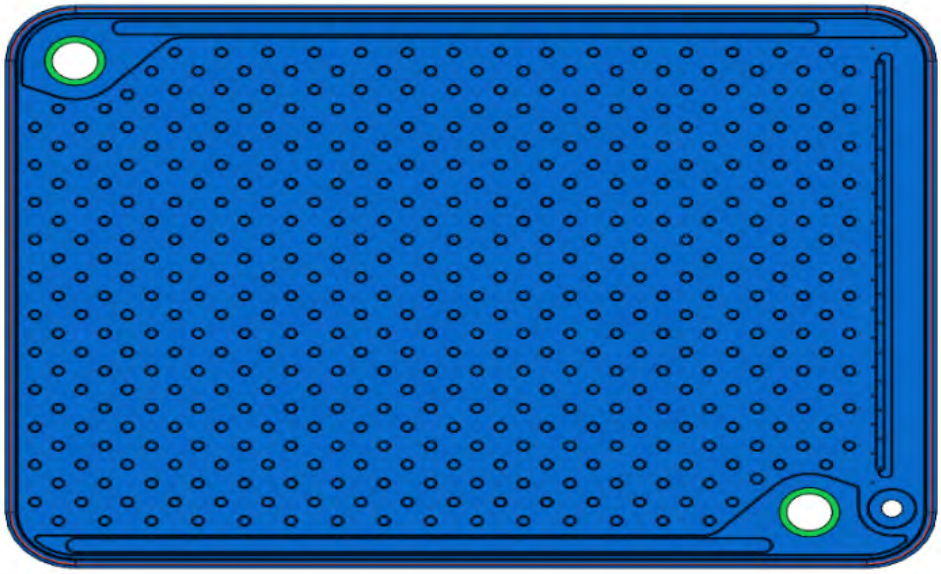

Figure 2.—CHX surface with convex dimples (Ref. 2).

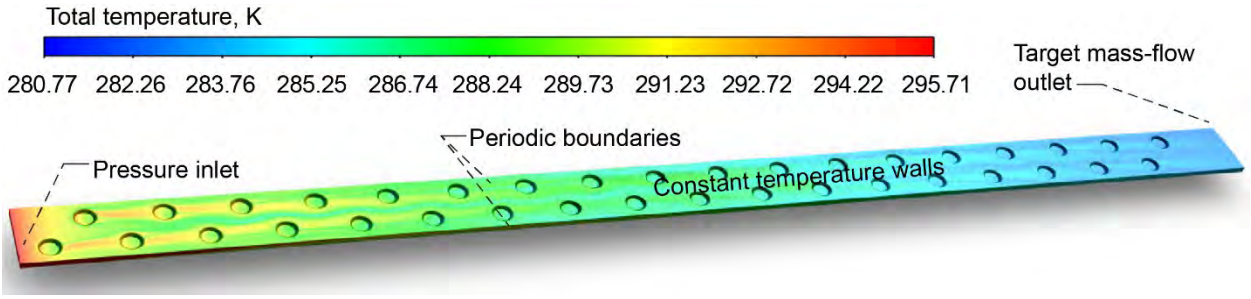

Figure 3.—Temperature conditions of dimpled surface; inlet at 103.214 kPa and 295.71 K, outlet at 0.0092856 g/s, wall settings at 280.28 K, and operating pressure at 101.325 kPa (Ref. 2).

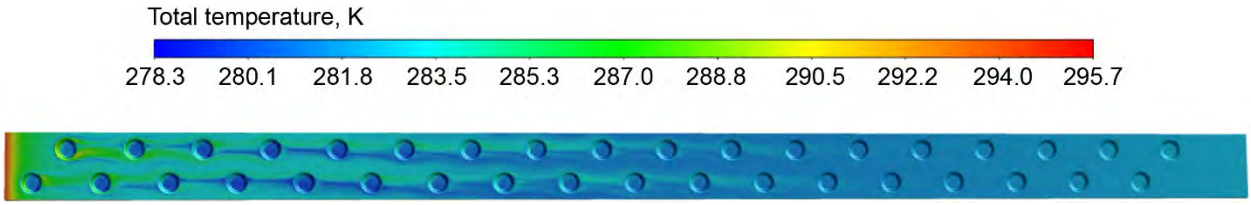

Figure 4.—Temperature conditions, top view (Ref. 2).

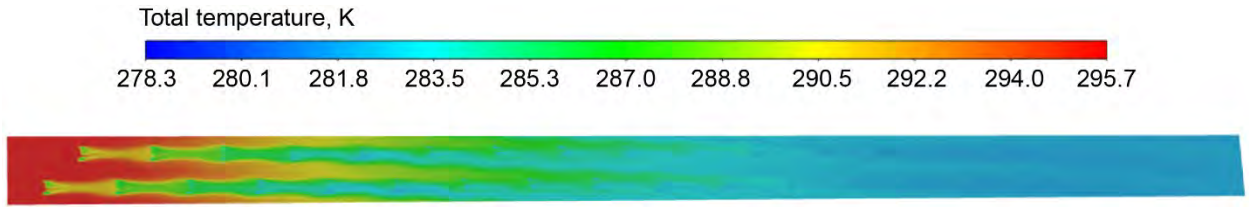

Figure 5.—Temperature conditions, top view; non-dimple imaging (Ref. 2).

3.2 Numerical Model

As part of this effort, a numerical model was developed to size and evaluate the performance of this CHX. Initially, two approaches were considered, one involving a thick condensation film on the HX, which inhibited heat transfer during air condensation, and another using a thin film that did not obstruct the heat transfer. Experimental analysis revealed a low enough condensation rate to make the thin film model a more accurate representation of the HX's behavior.

In the numerical model, individual channels were divided into 1-in.-wide (2.2-cm) cells with calculations progressing step-by-step to determine the initial temperature through an enthalpy balance. From this, pressure drop, heat transfer rate, and condensation rate were computed, using assumed flat-plate correlations for pressure drop and heat transfer within the channels. However, experimental results showed higher pressure drops than predicted. To enhance the accuracy and account for actual geometric features, CFD simulations were conducted, yielding more precise values for pressure drop and Nusselt numbers, which were then integrated back into the numerical model balances.

Initial plans were for the CHX unit to undergo laser processing of the dimpled surface to increase wettability and enhance the condensation process. As a result of the laser processing, the surface height and thermal resistance slightly changed; a second analysis layer was therefore applied in the numerical model to account for the new thermal resistance based on known properties of the processing method (Ref. 5).

3.3 Computational Fluid Dynamics

To minimize computational effort and simplify mesh resolution, a periodic section of a single channel was analyzed. Pointwise® software (Cadence Design Systems, Inc.) was used to create two configurations: a nondimpled channel with 2,521,950 nodes and a dimpled channel that contained 14,901,375 nodes. These extra-fine meshes were exported to Fluent® software (Ansys, Inc.), where CFD simulations were conducted in Ansys® Fluent® 2021 utilizing the shear stress transport (SST) k-ω turbulence model (Ref. 6).

Boundary conditions included a velocity inlet and a pressure outlet, both informed by the numerical model. Convergence was reached by reducing residuals by three orders of magnitude. A middle section of a channel, modeled with periodic boundaries (Figure 6), was used to calculate pressure drop and heat transfer, which were then extrapolated to represent the entire HX, shown in Figure 7 and Figure 8.

As shown in Figure 8, the SST *k*-ω and transitional models were in good agreement, and the laminar pressure model showed similar trends, indicating that any of them would be suitable for representing the flow for pressure drop calculations. The laminar velocity model was added because it showed better agreement than the pressure model. The geometry without dimples was also run as a control case in the SST *k*-ω model (Figure 7).

To verify that CFD results were independent of the mesh, a secondary coarser mesh with 2,101,545 cells was created, significantly reducing the cell count from that of the extra-fine mesh used in the previous simulations. CFD simulations were performed to meet a similar convergence criterion. As seen in Table I, the coarser mesh showed an average heat flux difference of 3.3%, a 5.1% variation in the Nusselt number, and a 1.1% difference in total pressure drop from inlet to outlet. Given that these differences were generally within 5%, it was concluded that the results from the extra-fine mesh were mesh independent. This confidence in the mesh sizing was reinforced as CFD results aligned with textbook calculations for a flat channel (Ref. 7). Computational time did not justify reducing node count further, as the increased count was necessary to accurately resolve the dimples.

The HX required to optimize LP-CHX performance for flight implementation would need to fit within current ISS ECLSS pressure operating parameters and be capable of the same power output as current state-of-the-art equipment. Key parameters were a targeted pressure drop of 248.84 Pa and a 4.192-kW output (Figure 7) (Ref. 2).

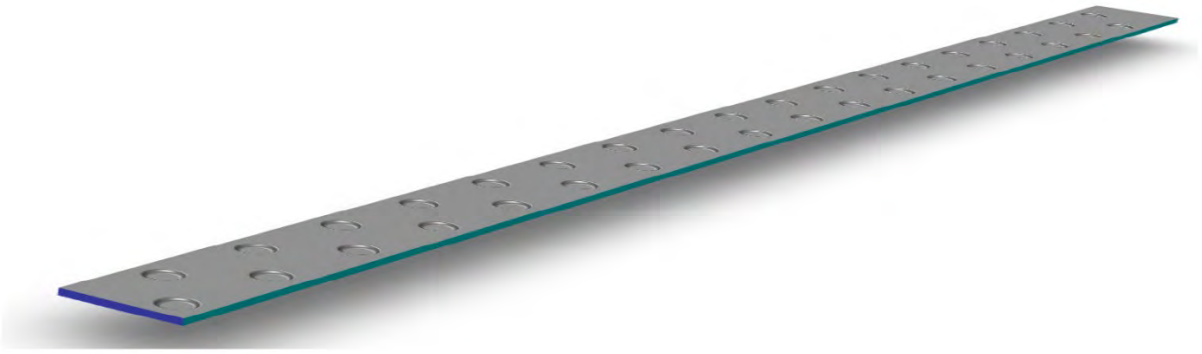

Figure 6.—Sliced view of dimpled surface used for modeling (Ref. 2).

TABLE I.—MESH INDEPENDENCE STUDY:
CHANGE IN KEY PERFORMANCE INDICATORS

Key Performance Indicator (KPI)	Percentage of extra-fine amount
Number of mesh cells	14.0
Average heat flux	3.3
Nusselt number	5.1
Total pressure drop	1.1

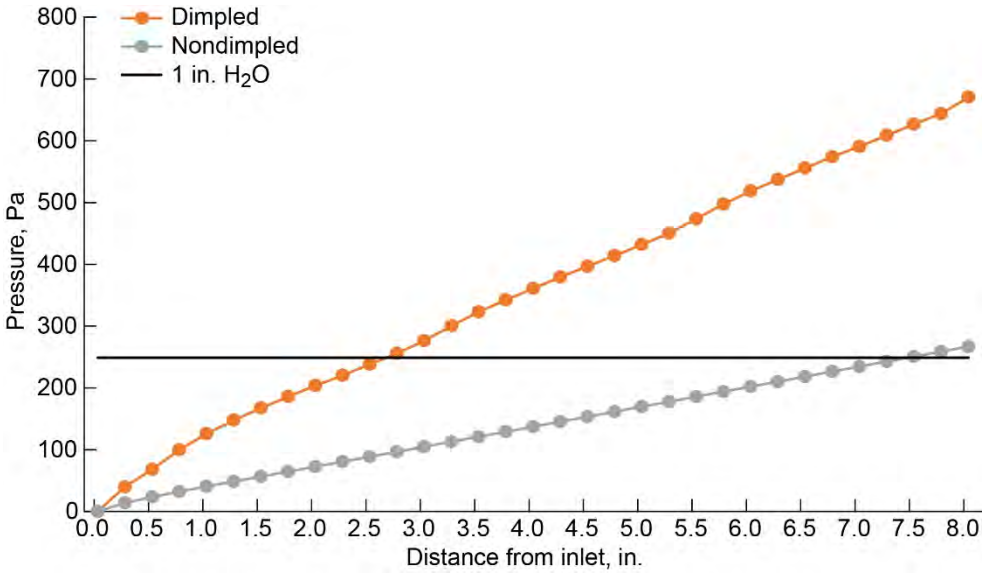

Figure 7.—Pressure drop from inlet; dimpled and nondimpled analysis using SST *k*-ω model; target threshold line for pressure drop on flight is 248.84 Pa for 1 in. of H_2O (Ref. 2).

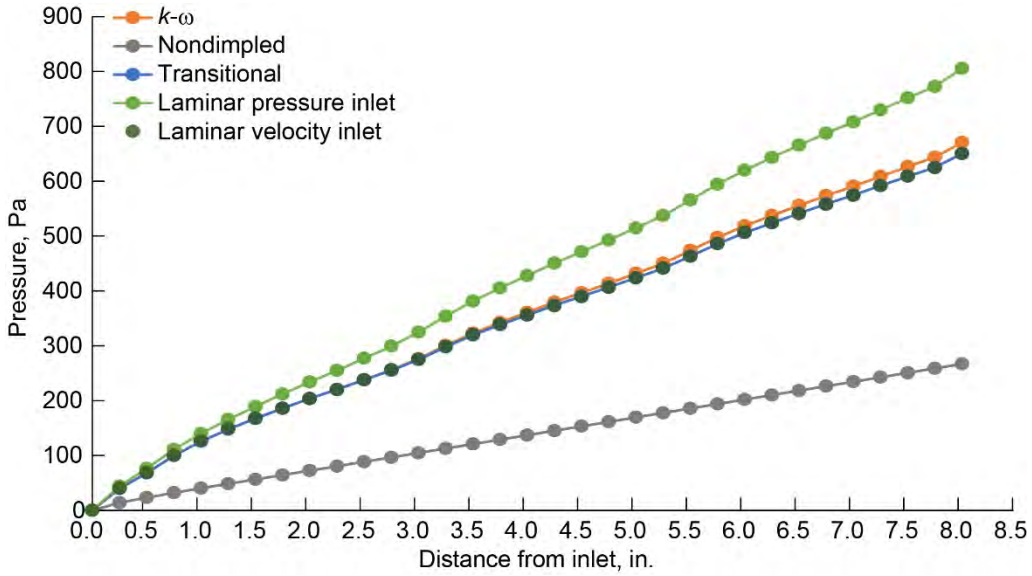

Figure 8.—CHX pressure drop versus distance from inlet for various models (Ref. 2).

3.4 Flow Characterization

The Reynolds number found was 1254.1, which slightly exceeded the threshold for internal flow to be classified as laminar. Consequently, the HX Nu was evaluated using a laminar model, a transitional model, and several turbulence models, as illustrated in Figure 9 and Figure 10; the peaks at the inlet for local Nu were due to flow instabilities at the model inlet. The SST *k*-ω and laminar models showed good agreement, as seen in Figure 10; however, the laminar flow model slightly underestimated Nu as compared to the turbulent case. Figure 11 displays the total heat transfer compared to the total pressure drop across the entire channel for all four scenarios originally tested.

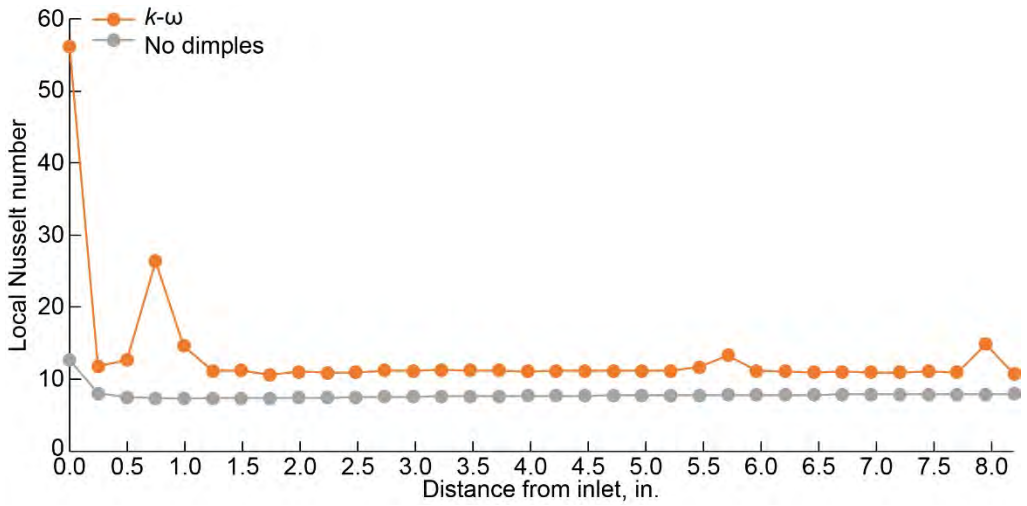

Figure 9.—CHX Nusselt number for SST *k*-ω model with and without dimples (Ref. 2).

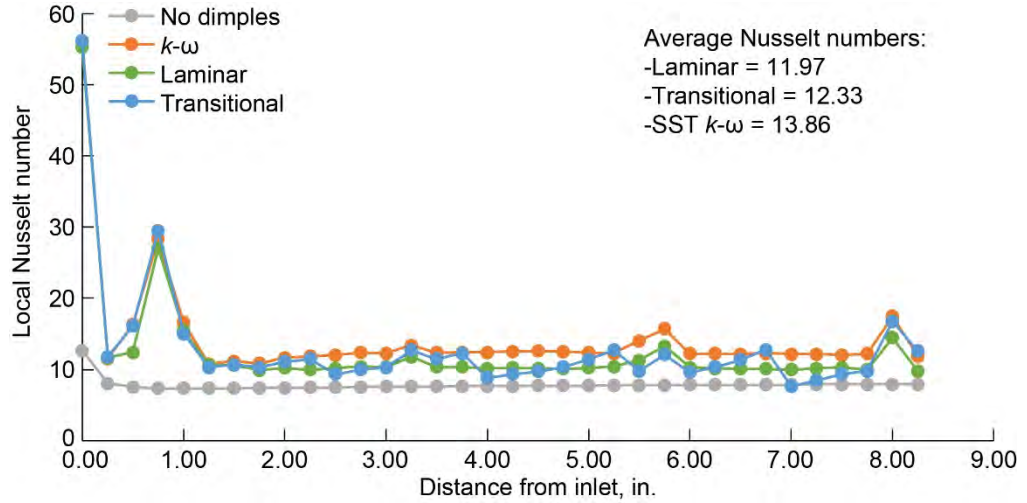

Figure 10.—CHX Nusselt number for various models; prior work without dimpled pattern shown for comparison using SST *k*-ω model (Ref. 2).

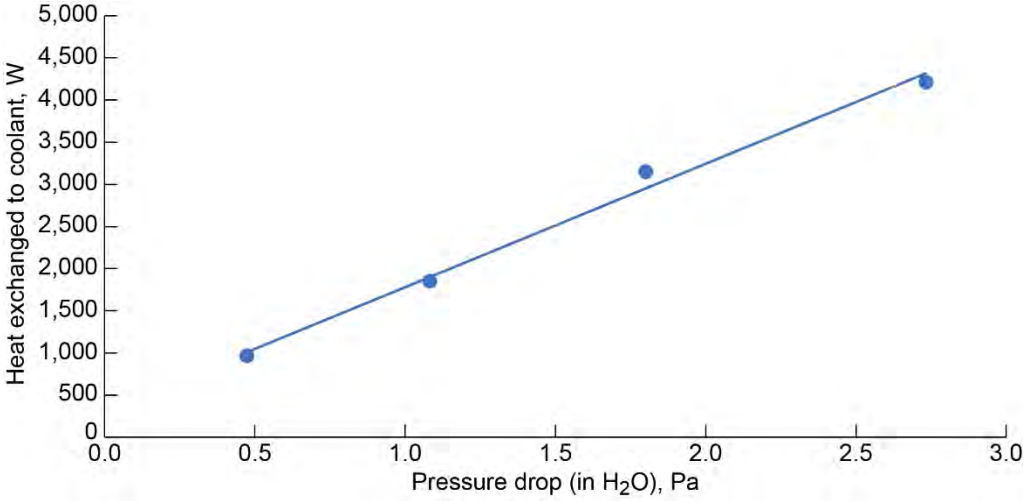

Figure 11.—CHX total heat exchanged versus total pressure drop for four loading cases (Ref. 2).

3.4.1 Reynolds Number Calculations

To find the Reynolds number, Re, the hydraulic diameter, D_h, was found:

$$D_h = \frac{4A}{P} \tag{1}$$

where the area of the hydraulic, A, is multiplied by 4 before being divided by the perimeter of the hydraulic, P, to get a total hydraulic diameter of 0.001889 m.

Using Equation (2), Re was calculated using a ρ of 1.225 kg/m^3, an averaged x-direction velocity (u) of 9.7 m/s, and a dynamic viscosity (μ) of 0.0000179 Pa·s. The calculation for this is

$$\mathrm{Re_x} = \frac{\rho \times u \times D}{\mu} \tag{2}$$

In small channels, a Reynolds number of 3,000 to 4,000 is traditionally considered turbulent. However, this does not consider surface effects; a flow in transition can be tripped into turbulence, which generally is the purpose of the dimples. CFD confirmed that a nonlaminar mixing was occurring. Therefore, the calculated Reynolds number here of 1254.1 warranted several additional models showing laminar, transitional, and turbulent modeling to find the most representative case.

3.4.2 Nusselt Number Calculations

Using Python postprocessing script, the Nusselt number was calculated in this experiment as a dimensionless number that represents the ratio of convective to conductive heat transfer at a wall boundary within the fluid. Both advection (fluid motion) and diffusion (conduction) were included in the calculations, chosen to represent the overall performance profile of the system. The heat transfer coefficient, h, was calculated using Equation (3), where T is temperature, T_w is wall temperature, q'' is heat flux, k is thermal conductivity, **N** is normal vector to the wall, and T_{ref} is reference temperature. The variable T_{ref} can be chosen arbitrarily but must be kept consistent, as shown in Equation (4), where C_p is specific heat capacity at constant pressure, **U** is velocity vector, A is area, and d is depth of penetration. When using Ansys® Fluent® software, T_{ref} defaults to a constant value, but for this study, T_{ref} was calculated as the bulk fluid temperature along the length (L) of the HX.

$$h = \frac{q''}{T_w - T_{ref}} = \frac{-k\frac{\partial T}{\partial n}\Big|_{at\ wall}}{T_w - T_{ref}} \tag{3}$$

Where

$$T_{ref} = \frac{\iint \rho C_p u T dA}{\rho C_p \mathbf{U} A} \tag{4}$$

The average Nusselt number, $\overline{\mathrm{Nu}}$, was calculated using Equation (5), which includes the average heat transfer coefficient, $\bar{h}$, determined via integration in Equation (6).

$$\overline{\mathrm{Nu}} = \frac{\bar{h} D_h}{k} \tag{5}$$

Where

$$\bar{h} = \frac{1}{L}\int_0^L h(x)\, dx \tag{6}$$

Ansys® Fluent® was used to solve these equations along the length of the slice. The prior model was updated with the calculated Nusselt number, and a macro script was run to provide the condensation rate and the heat transferred to the cooling fluid (Ref. 2).

These simulations provided detailed calculations of heat flux and pressure drop within the channels, enabling the derivation of localized Nusselt numbers and the inclusion of dimple-induced pressure drop adjustments in the numerical model. Moreover, incorporating precise geometric measurements from drafting software further enhanced the fidelity of the numerical model, ensuring a more accurate representation of the HX's performance.

Images of the Python postprocessing script can be found in Appendix B (Figure 76).

4.0 Work Performed at University of Nebraska-Lincoln

The work completed by University of Nebraska-Lincoln (UNL) sought to determine the efficiency of FLSP to create an antimicrobial surface similar to ones previously completed in the same manner, but at much higher processing rates. The CHX design and any changes were cross referenced with FLSP standards to ensure compliance before demonstrating the laser technique and exploring potential options for reduced manufacturing time of a full-scale LP-CHX.

4.1 Microscopy Studies

To supplement the modeling efforts, additional work was performed to determine the efficacy of laser processing to functionalize electroplated silver and create similar antimicrobial surfaces as in previous work. This was performed by UNL with their Center for Electro-Optics and Functionalized Surfaces (CEFS) laboratory. Here, FLSP is used to create self-assembly of unique structures contributing to the enhanced fluid-control properties.

The mission of CEFS, an internationally recognized research center, is to provide services to those in the State of Nebraska and the Nation in metallic surface functionalization and ultrafast surface characterization, or pump-probe characterization (Ref. 8). Comprising more than 30 individuals from a range of disciplines, CEFS is a collaborative research group with state-of-the-art facilities.

CEFS was able to verify the reported electroplated silver thickness through two separate microscopy processes while providing evidence against plating penetration and delamination. It was here that options for reduced manufacturing time were explored and a full-scale electroplated packet was processed.

4.2 Thickness of Electroplated Samples

UNL used the electroplated materials received from two vendors to complete a thickness analysis on the electroplated silver. Two distinct methods were used for this analysis. There was a disproportion of samples because Vendor 1 provided more samples and data than Vendor 2 did.

The first method required samples to be cut from the electroplated silver using electrical discharge machining (EDM), followed by scanning electron microscope (SEM) imaging and backscattered electron detection imaging (BSED). This combination showed a high-resolution contrast between the stainless steel and the electroplated silver layer. The EDM-cut samples were rough and melted; the result was a

mix of silver and stainless steel that required the faces of the cuts be hand polished with fine grit sandpaper before imaging. Examples of the raw and polished cuts can be found in Figure 12.

Figure 13 to Figure 19 show examples of measurements made from the EDM SEM technique, using different thicknesses and materials from each vendor. All SEM images were taken at ×1,000 magnification unless otherwise specified. Figure 16 and Figure 18 show part of the sample labeled “location 1,” where minimum thickness was 113 µm, maximum thickness was 171 µm, and average thickness was 142.02 µm. Figure 17 and Figure 19 show part of the sample labeled “location 2,” where minimum thickness was 116 µm, maximum thickness was 179 µm, and average thickness was 143.71 µm.

Figure 20 provides an example of measurement locations, and Figure 21 to Figure 24 provide a summary of the thickness measurements based on a greater set of measurements than previously shown. These are used to show plating consistency across the packet. Only Vendor 1 reported thickness for samples, as they were the only vendor whose equipment could measure thicknesses up to the specified units.

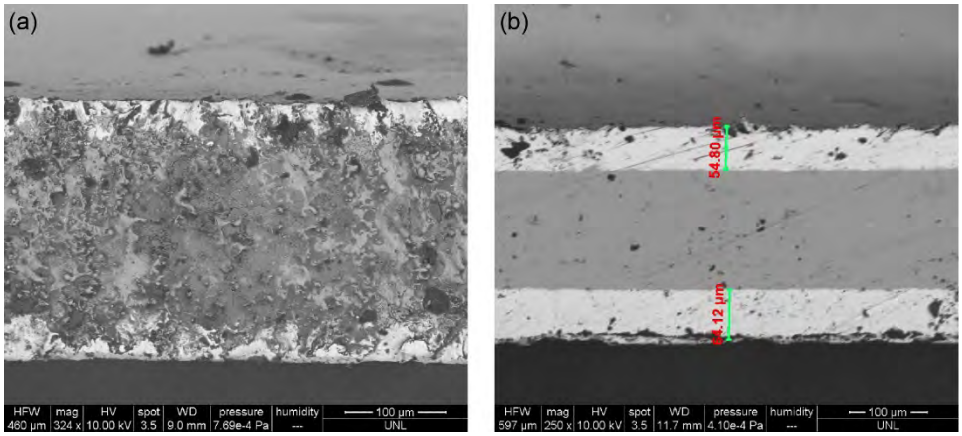

Figure 12.—Examples of electroplated silver cross sections before and after polishing. (a) Raw cut. (b) Polished.

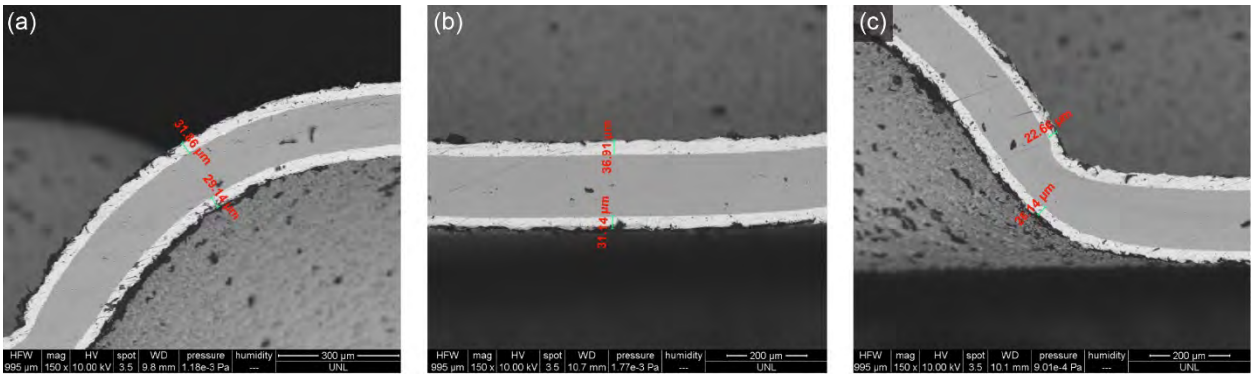

Figure 13.—Vendor 2 sample at 76 µm specified thickness. (a) Dimple top edge. (b) Unstamped. (c) Dimple lower edge.

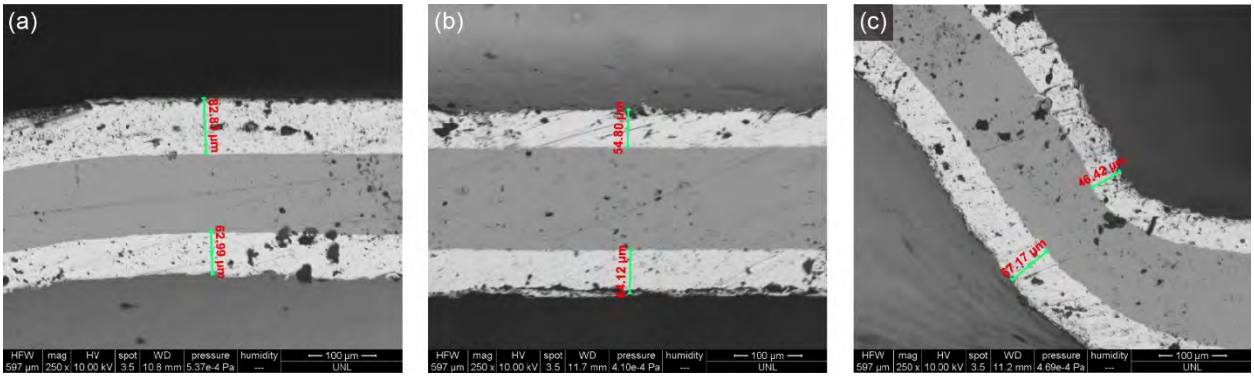

Figure 14.—Vendor 1 sample at 76 μm specified thickness. (a) Dimple top edge. (b) Unstamped. (c) Dimple lower edge.

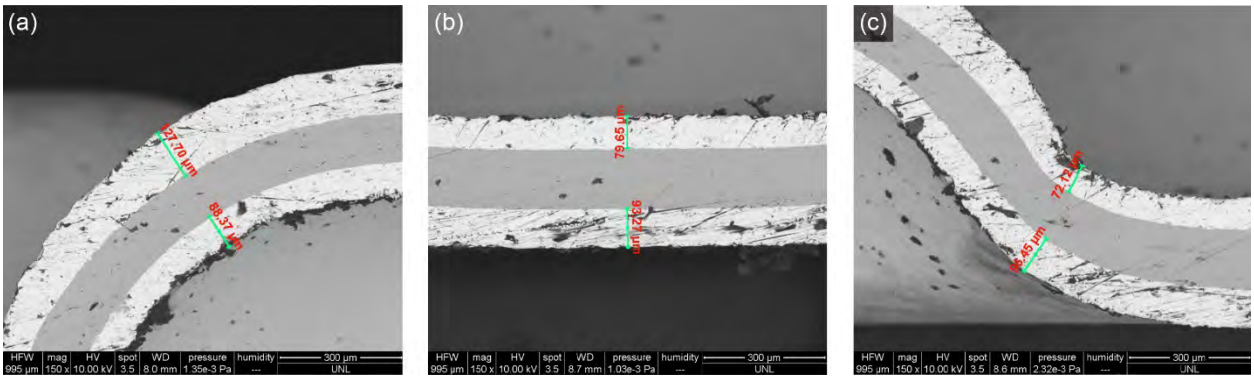

Figure 15.—Vendor 1 sample at 102 μm specified thickness. (a) Dimple top edge. (b) Unstamped. (c) Dimple lower edge.

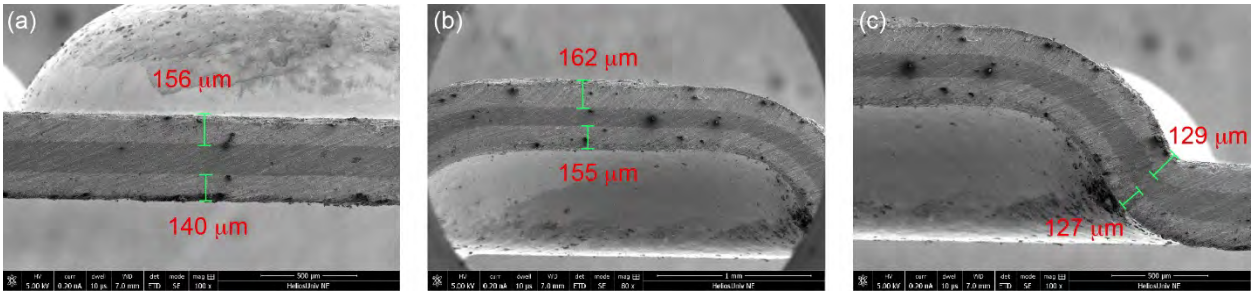

Figure 16.—Vendor 1 sample at 127 μm specified thickness (location 1). (a) Stamped edge. (b) Upper dimple top edge. (c) Side edge of dimple.

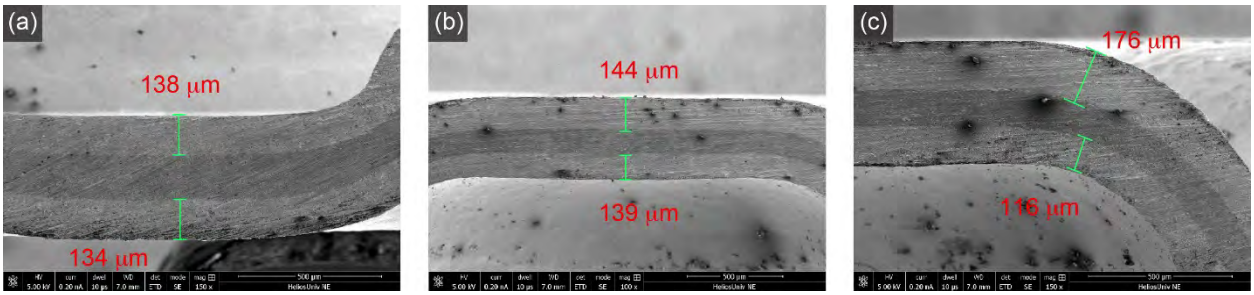

Figure 17.—Vendor 1 sample at 127 μm specified thickness (location 2). (a) Stamped edge. (b) Upper dimple. (c) Side edge of dimple.

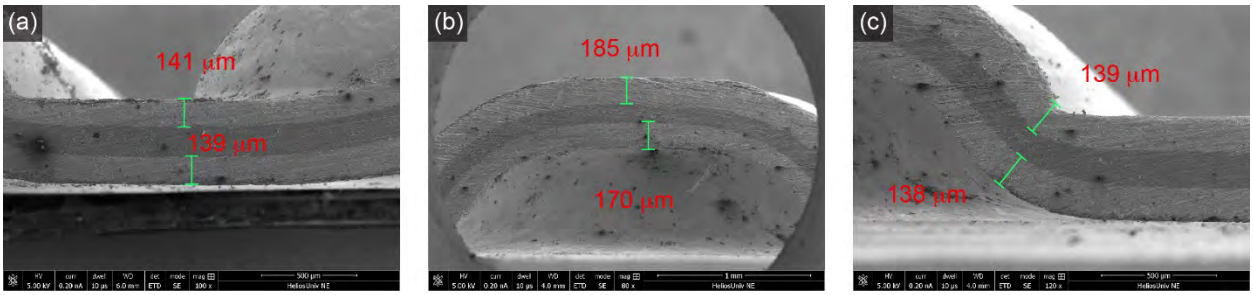

Figure 18.—Vendor 1 sample at 152 μm specified thickness (location 1). (a) Stamped edge. (b) Upper dimple top edge. (c) Side edge of dimple.

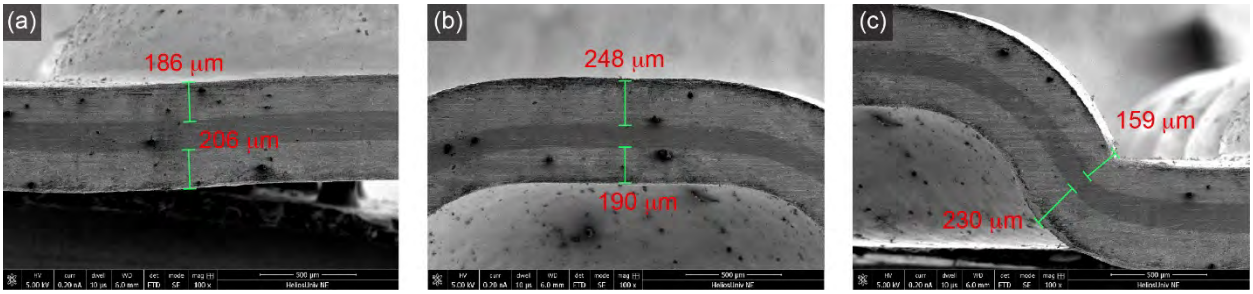

Figure 19.—Vendor 1 sample at 152 μm specified thickness (location 2). (a) Stamped edge. (b) Upper dimple top edge. (c) Side edge of dimple.

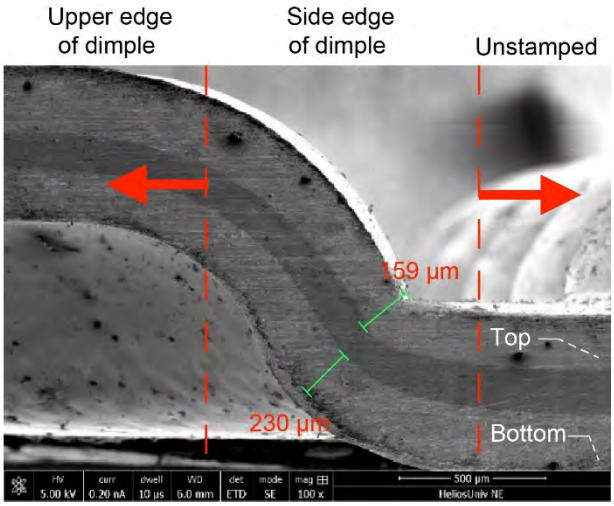

Figure 20.—Example of measurement locations.

Sample no. (a)	Upper dimple (top/bottom), µm	Upper dimple (top/bottom), µm	Unstamped (top/bottom), µm	Average, µm	Std. deviation, µm
1	169.83 / 137.16	178.83 / 172.16	136.83 / 148.83	157.27	22.32
2	181.83 / 179.5	239.33 / 181.33	182.5 / 196.5	193.49	23.62
3	166.5 / 147.16	212.83 / 197.83	185.16 / 163.66	178.85	26.46
4	159.83 / 158.8	188.16 / 157.33	154.16 / 177.5	165.96	18.68
5	216.5 / 233	239.5 / 186.33	175.5 / 194	207.47	37.52

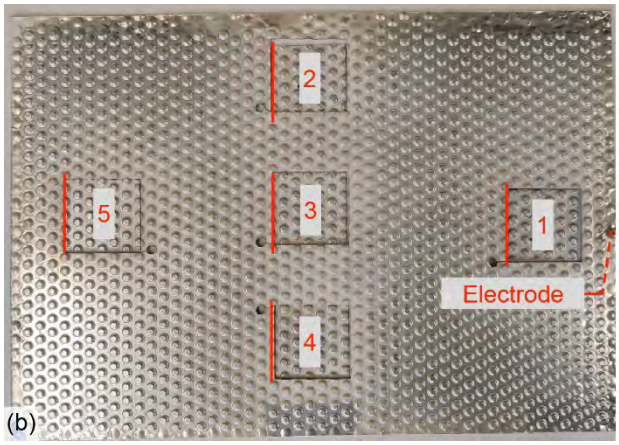

Average measured thickness = 180.6 µm (7.11 mil)
Minimum measured thickness = 137 µm (5.39 mil)
Maximum measured thickness = 240 µm (9.45 mil)

Figure 21.—Thickness measurements for five locations on electroplated silver from Vendor 1 at 152 µm specified. (a) Table of thickness measurements. (b) Measurement locations.

Sample no. (a)	Upper dimple (top/bottom), μm	Upper dimple (top/bottom), μm	Unstamped (top/bottom), μm	Average, μm	Std. deviation, μm
1	156.66 / 154.33	130.83 / 134.16	137.16 / 139	142.02	13.42
2	166 / 131.66	167 / 127.66	131 / 139	143.71	17.95
3	145 / 107.5	130.83 / 105.5	97.16 / 110	115.99	18.60
4	151.16 / 102	107.83 / 94.83	97.55 / 118.16	111.93	22.47
5	169.83 / 135.16	157.15 / 136.5	156.33 / 229.66	164.1	36.51

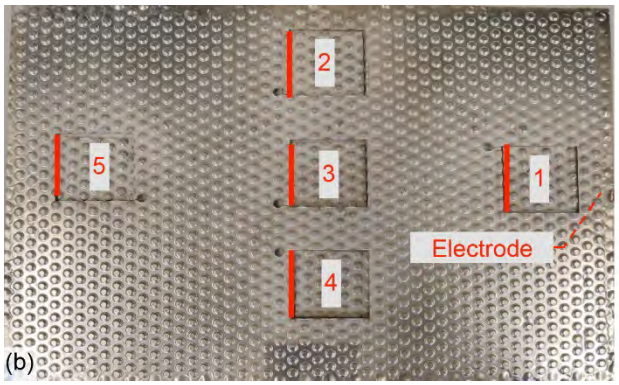

Average measured thickness = 135.5 μm (5.33 mil)
Minimum measured thickness = 97 μm (3.82 mil)
Maximum measured thickness = 230 μm (9.06 mil)

Figure 22.—Thickness measurements for five locations on electroplated silver from Vendor 1 at 127 μm specified. (a) Table of thickness measurements. (b) Measurement locations.

Sample no. (a)	Upper dimple (top/bottom), μm	Upper dimple (top/bottom), μm	Unstamped (top/bottom), μm	Average, μm	Std. deviation, μm
1	119.73 / 74.61	59.07 / 85.18	76.91 / 80.15	82.61	18.44
2	148.58 / 93.08	94.56 / 114.18	94.39 / 115.56	110.05	19.61
3	127.70 / 88.37	72.12 / 96.45	79.65 / 93.27	92.93	17.57
4	138.38 / 85.61	75.44 / 108.03	87.42 / 112.69	101.26	21.05
5	166.99 / 109.48	97.00 / 91.33	99.08 / 114.62	113.03	25.33
6	130.18 / 100.44	88.09 / 114.15	114.62 / 119.48	111.16	13.53
7	112.13 / 88.22	71.49 / 98.41	91.37 / 106.89	94.75	13.28
8	255.89 / 173.41	113.84 / 249.64	183.60 / 216.62	198.83	48.74
9	208.08 / 115.56	90.19 / 148.39	117.54 / 144.74	137.42	37.13

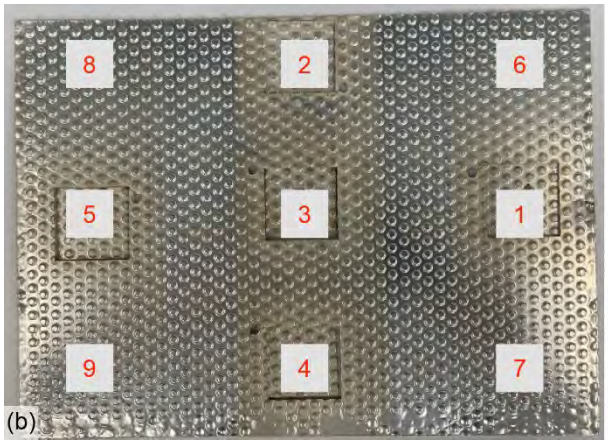

Manuf. reported thickness = 112.8 μm (4.44 mil)(σ = 0.004)
Average measured thickness = 115.8 μm (4.56 mil)(σ = 1.66)
Minimum measured thickness = 59 μm (2.32 mil)
Maximum measured thickness = 255.9 μm (10.07 mil)

Figure 23.—Thickness measurements for nine locations on electroplated silver from Vendor 1 at 102 μm specified. (a) Table of thickness measurements. (b) Measurement locations.

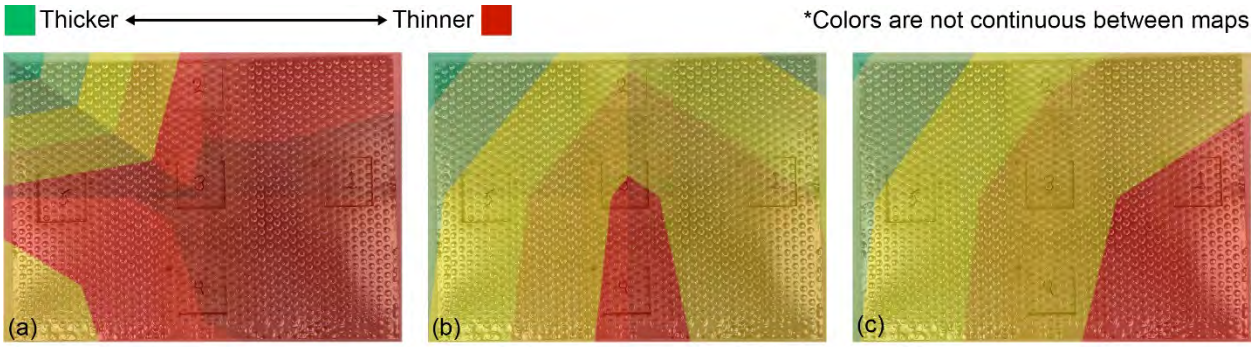

Measured	Measured	Measured
Average: 4.56 (115.79 μm)	Average: 5.34 (135.52 μm)	Average: 7.11 (180.60 μm)
Standard deviation: 1.66 (42.08 μm)	Standard deviation: 1.10 (27.82 μm)	Standard deviation: 1.06 (26.86 μm)
Minimum: 2.33 (59.07 μm)	Minimum: 3.73 (94.83 μm)	Minimum: 5.39 (136.83 μm)
Maximum: 10.07 (255.89 μm)	Maximum: 9.04 (229.66 μm)	Maximum: 9.43 (239.50 μm)

Figure 24.—Visual comparison of coating thickness on Vendor 1 materials based on EDM and SEM; three representative images were used to create maps at various points across entire surface. (a) Map 1. (b) Map 2. (c) Map 3.

The second method used for measuring thickness of the electroplated silver was x-ray computed tomography (XCT). XCT requires little to no sample preparation, is entirely nondestructive, provides an internal three-dimensional (3D) scan of the entire sample, and allows the viewer to see internal geometries with elemental contrast. However, its finite resolution can result in some blurring of material boundaries, and the thin material can cause artifacts such as voids and surface features to be seen in scans. This is evident in sample 1 from Vendor 1, which had a specified plating thickness of 76.2 μm. Vendor 1 provided XCT imaging from multiple angles to demonstrate the thickness uniformity throughout the sample (Figure 25). The voids and surface features are all imaging artifacts.

Figure 26 shows an enlarged view of one edge to differentiate between the silver coating and the stainless-steel substrate. As in Figure 25, the voids are artifacts of the XCT imaging. Figure 27 shows thickness measurements from sample 1 in terms of specific edge comparisons.

SEM and XCT imaging gave similar thickness results within the standard deviation. Each technique has advantages; SEM has a higher imaging resolution, whereas XCT can acquire larger measurement sets in a shorter timeframe. Ultimately, EDM+SEM measurements were preferred over XCT measurements. Vendor 1 consistently met or exceeded the requested plate thickness, though they struggled with consistency across packets and between batches. It was found that the minimum plating thickness always occurred on the dimples' outer edge where they met the unstamped materials.

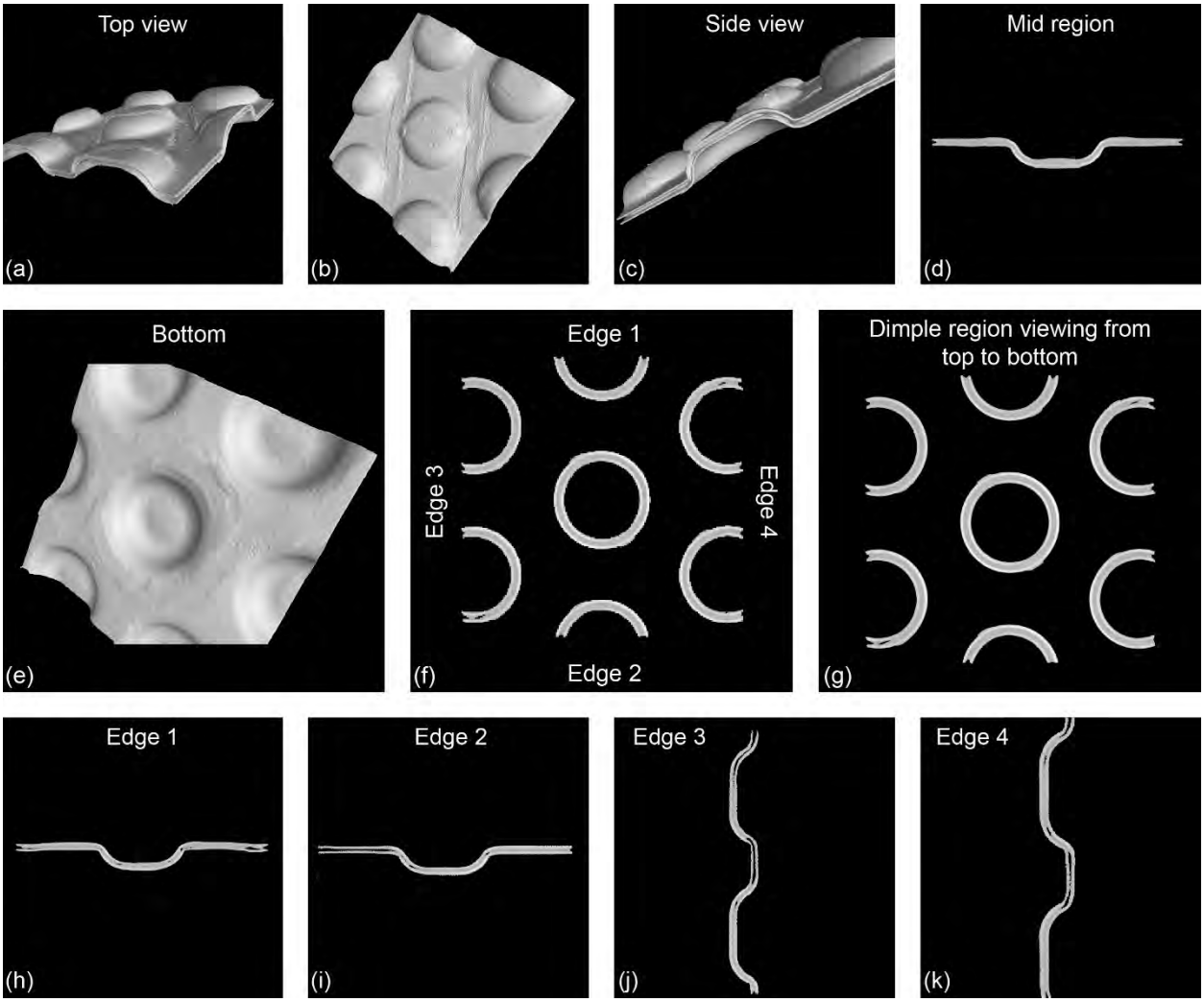

Figure 25.—All angles of XCT imaging of plate from Vendor 1 at 76.2 µm. (a) and (b) Top view. (c) Side view. (d) Mid region. (e) Bottom. (f) and (g) Dimple regions, top to bottom. (h) Edge 1. (i) Edge 2. (j) Edge 3. (k) Edge 4.

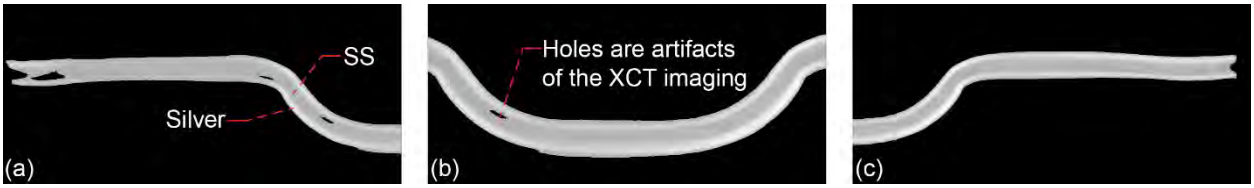

Figure 26.—Enlarged XCT imaging of Vendor 1 thickness at 76.2 µm. (a) Left side; stainless steel, SS. (b) Mid region. (c) Right side.

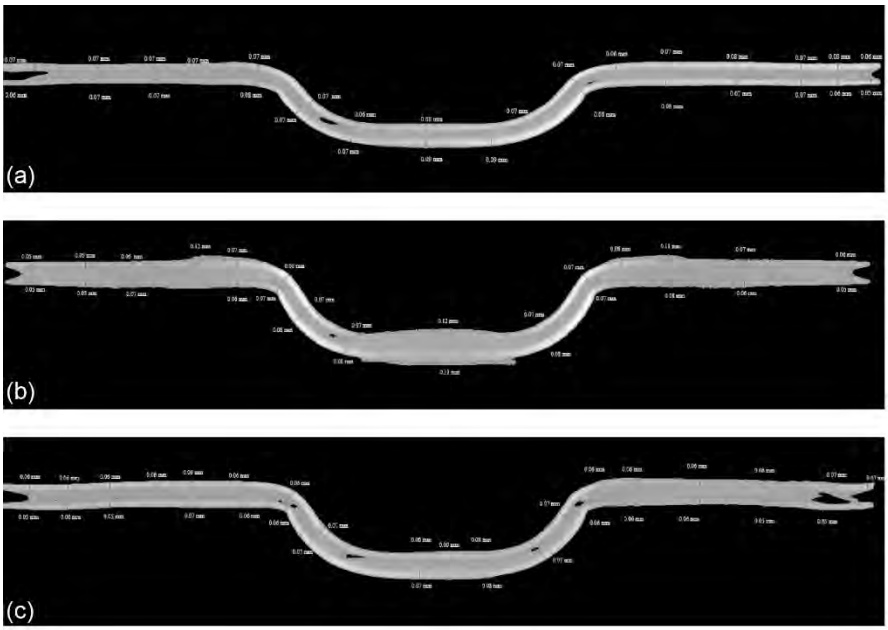

Figure 27.—Vendor 1 sample 1 edge thickness measurements. (a) Edge 1. (b) Middle. (c) Edge 2.

4.3 Applying Femtosecond Laser Surface Processing to Electroplated Surfaces

FLSP is a refined technique used to create the unique structures for microbial tolerance, as illustrated in Figure 28. Laser processing leads to self-assembly, in which microscopic mounds overlaid with nanoscale features form. These mounds are close enough together to prevent bacteria from adhering to the surface and leach large amounts of silver ions when exposed to condensate, killing any bacteria. The original dimple design was from a previous contract using 1/10th-scale units; however, it was observed that surfaces with an angle exceeding 45° prohibited uniform structuring, requiring a redesign to fit the project needs.

Both vendors were considered, but the biggest discrepancy came from the final surface finish; Vendor 1 provided a smooth and consistent finish, whereas Vendor 2 provided a rough surface that was sprinkled with silver nodules that would not support uniform FLSP. Because of this, the project team decided to exclude Vendor 2 from further consideration, making Vendor 1 the ideal contractor.

Figure 29 to Figure 31 show the refined laser processing parameters, provided to give a greater idea of the focal depth comparison between the positive dimple areas and the flat areas between the dimples. Figure 29 provides evidence of a lack of FLSP structures on sides with angles exceeding 45°.

A map of surface structures based on the sample surface location relative to the focus for electroplated silver helped find that over a 6-mm height range, there was very little change in FLSP features, providing an important result for processing nonflat packages with the same dimples (Ref. 9).

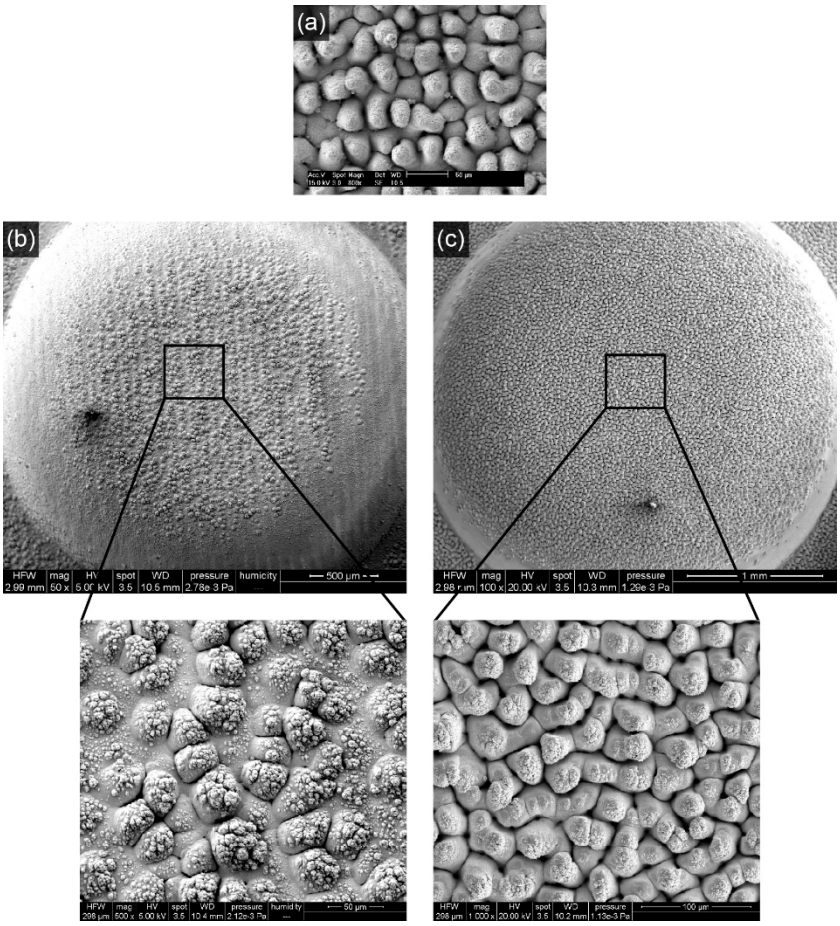

Figure 28.—Refined laser processing using coating from Vendor 1. (a) Target (used on 1/10th-scale unit). (b) Initial attempts. (c) Improved results.

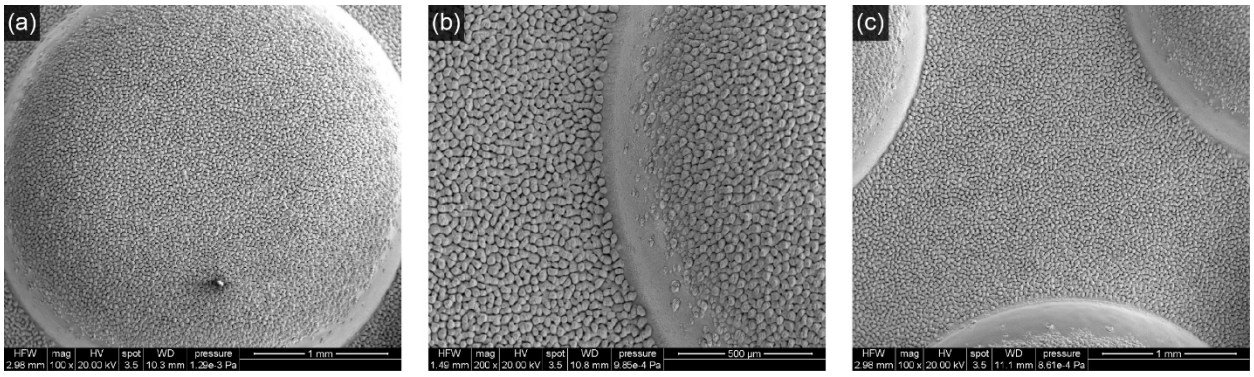

Figure 29.—Coating from Vendor 1 illustrating lack of FLSP structures on the dimple sides. (a) Positive dimple top. (b) Positive dimple edge. (c) Flat area.

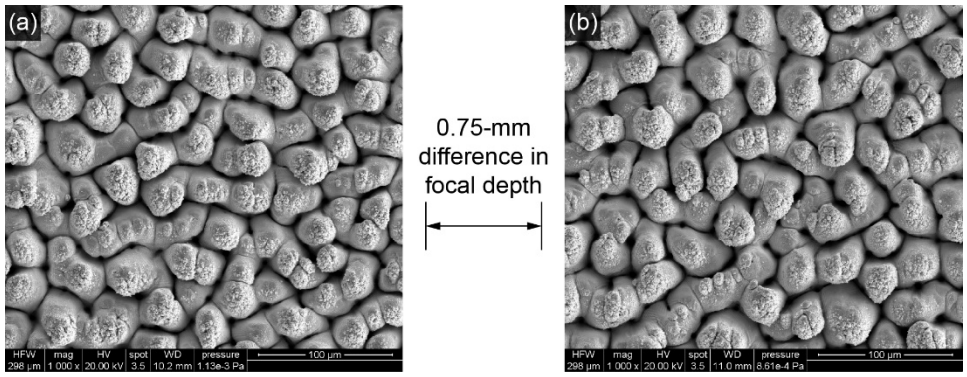

Figure 30.—SEM images of Vendor 1 coating showing 0.75-mm difference in focal depth. (1) Top of positive dimple; working distance (WD), 10.2 mm. (b) Flat area between dimples; WD, 11.0 mm.

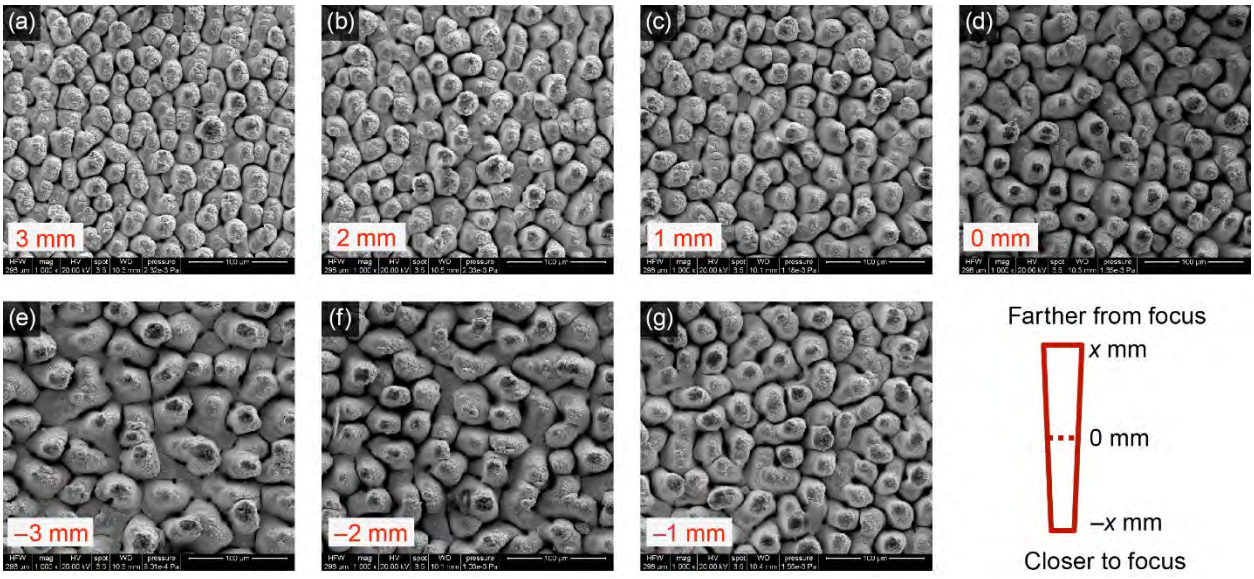

Figure 31.—Seven images of electroplated silver at varying WD. (a) 3 mm. (b) 2 mm. (c) 1 mm. (d) 0 mm. (e) –3 mm. (f) –2 mm. (g) –1 mm.

The second method of surface characterization, XCT analysis, allowed for data to be collected on unprocessed and FLSP-processed silver samples. However, the resolution was too low to see the individual FLSP microstructures, making the increased surface roughness only slightly visible. A comparison of unprocessed and FLSP-processed images is seen in Figure 32; the XCT energy and power settings were 210 kV and 35 W. This data collection also allowed for in-depth XCT analysis and measurements for the unprocessed (Figure 33 and Figure 34) and processed (Figure 35 and Figure 36) samples provided by Vendor 1, supplying evidence to support the study of silver plate thinning caused by FLSP.

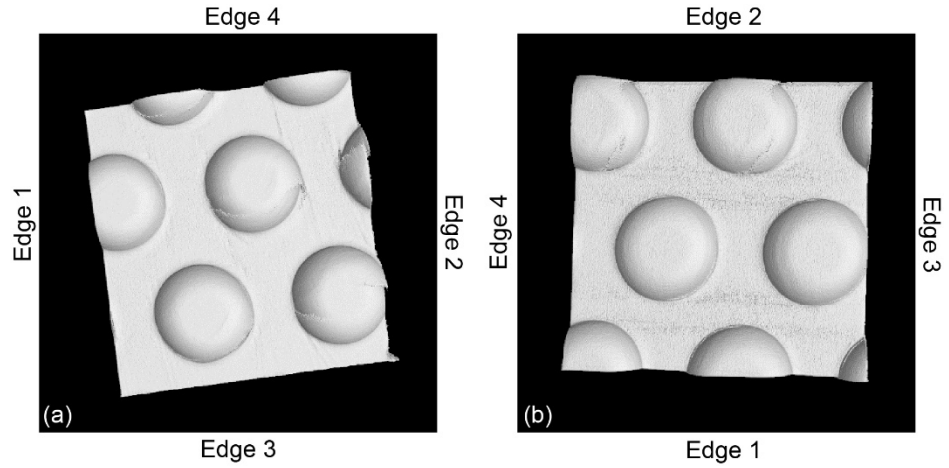

Figure 32.—XCT comparison of unprocessed and processed surfaces using Vendor 1 sample. (a) Unprocessed surface. (b) FLSP-processed surface.

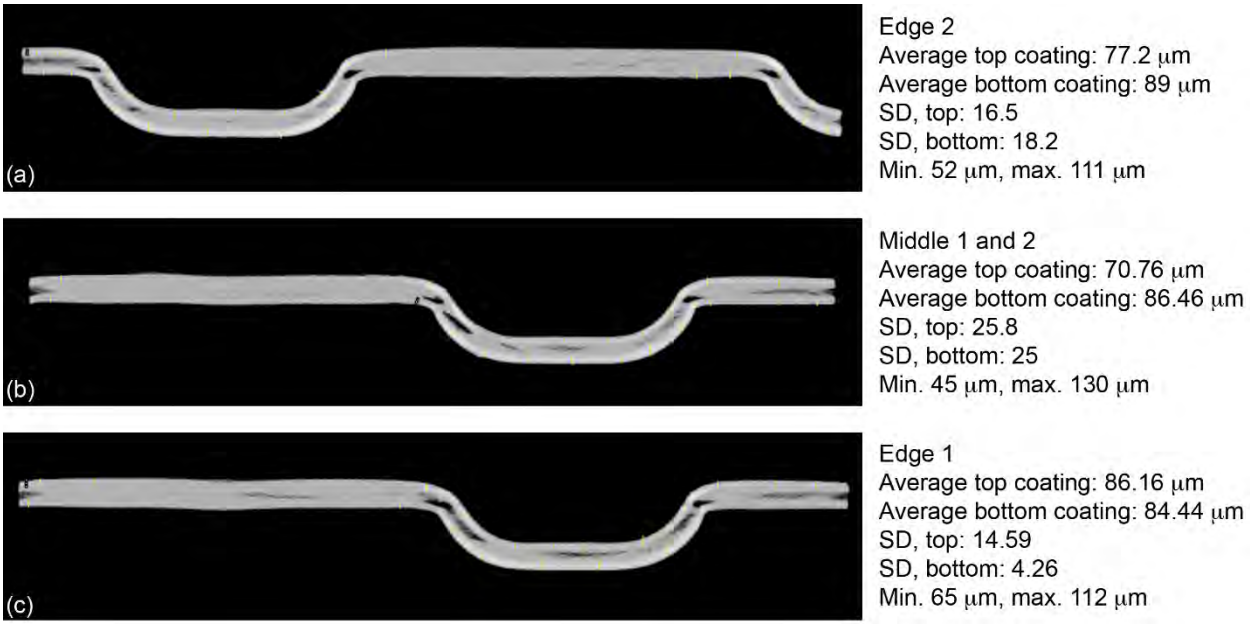

Figure 33.—Unprocessed sample. (a) Edge 2. (b) Middle 1 and 2. (c) Edge 1.

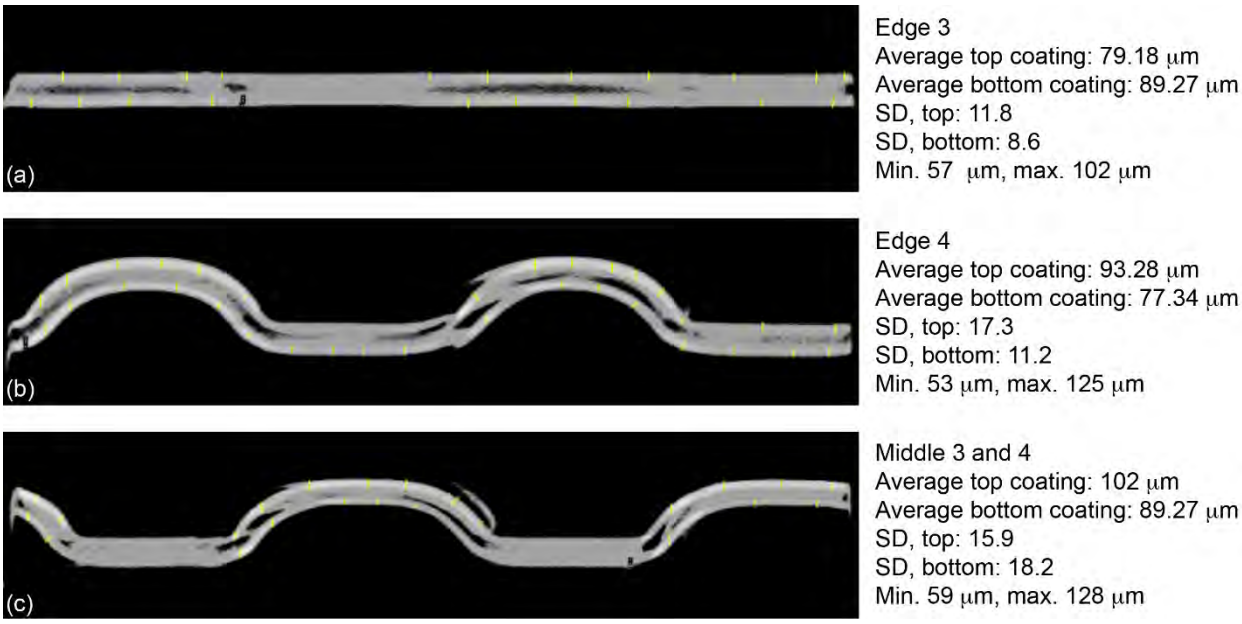

Figure 34.—Unprocessed sample. (a) Edge 3. (b) Edge 4. (c) Middle 3 and 4.

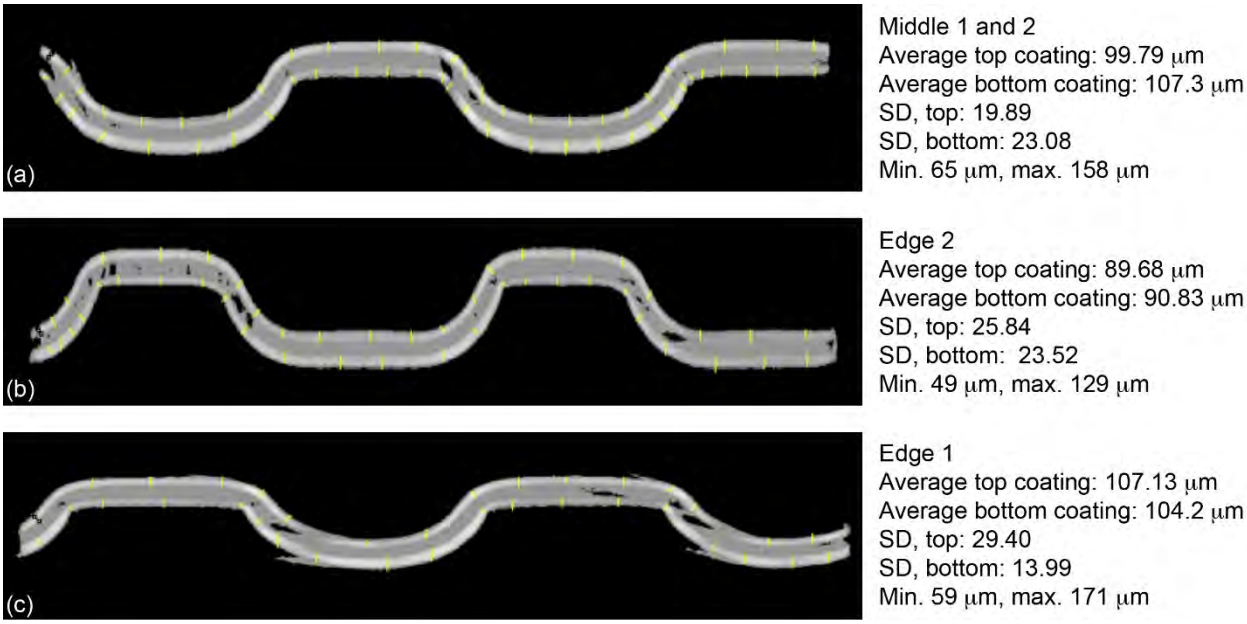

Figure 35.—Processed sample. (a) Middle 1 and 2. (b) Edge 2. (c) Edge 1.

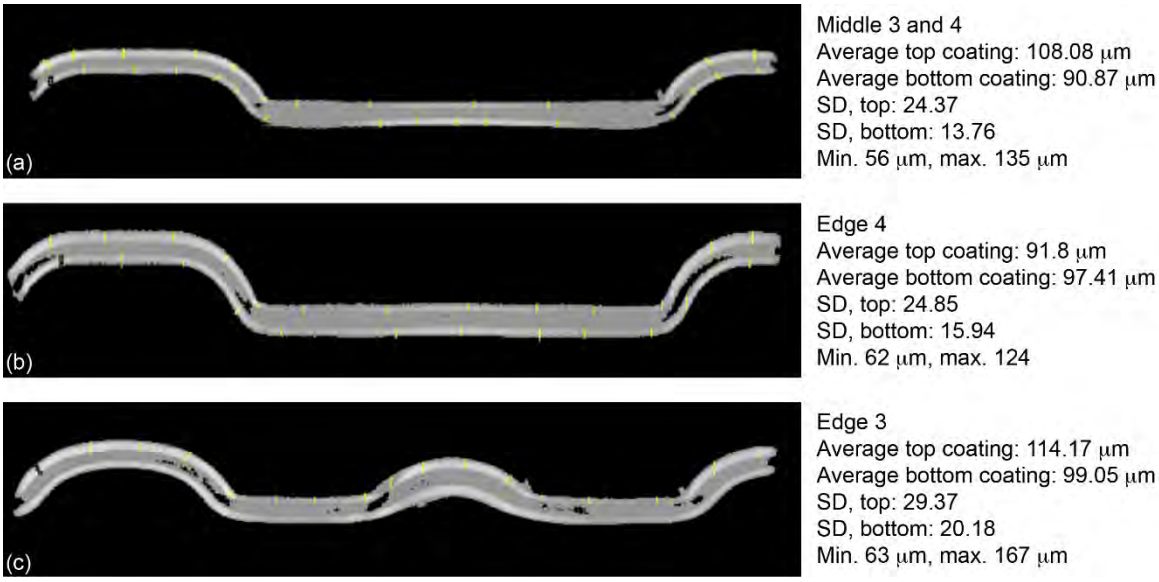

Figure 36.—Processed sample. (a) Middle 3 and 4. (b) Edge 4. (c) Edge 3.

This collection of data showed that dual-pulse FLSP-produced surface features are close to identical between electroplated silver and bulk silver from the 1/10th-scale CHX project. It was determined that packet features need to be redesigned so surfaces do not exceed a 45° angle relative to the surface normal. When using a 300-mm focal lens, height deviations of ±3 mm do not result in significant surface features.

4.4 Verification of Absence of Pinholes in Electroplated Samples As Received and After Applying FLSP

Energy-dispersive analysis via x-ray (EDAX) is an analytical method to quantify elements present in a sample material. It was used in this study to determine if there were pinholes in the sample after FLSP and to check for electroplated silver film continuity. If iron is not detected in the sample, this indicates that no pinholes were induced by FLSP.

EDAX positioning and results are shown in Figure 37 and Figure 38. For the processed sample in Figure 37, peak analysis showed Fe peaks located between 0.6 and 1 keV (L energy level) and between 6 and 7 keV (K energy level). Ag peaks were located between 2.8 and 3.5 keV (L) and between 0.05 and 0.5 keV (K).

EDAX area scans for processed samples are shown in Figure 39 to Figure 43.

An example of silver coating penetration by laser processing is shown in Figure 44, where maximum *d* is 56 μm. Maximum *d* is the depth of the lowest valley between microstructures relative to the unprocessed silver surface. Silver structure depths for various laser parameters are shown in Figure 45; maximum *d* is 48 μm. For both figures, 3D surface profile measurements were made using a Keyence® (Keyence Corp.) VK200 laser-scanning confocal microscope (LSCM).

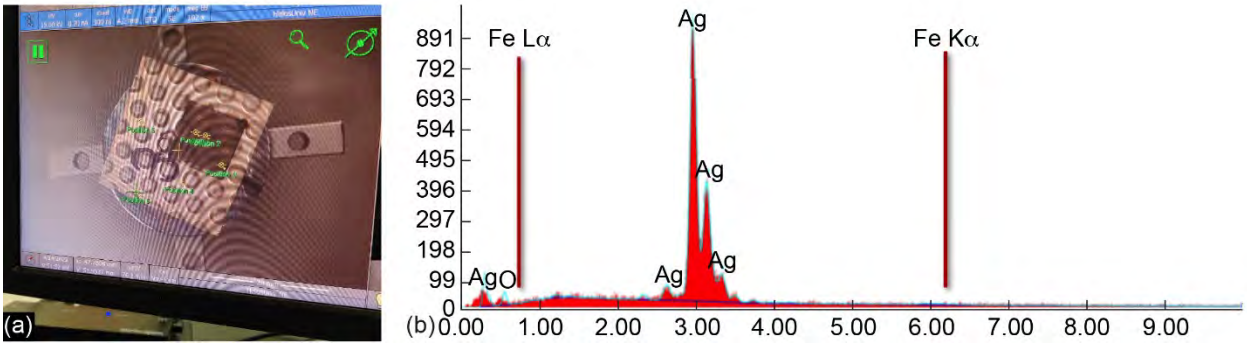

Figure 37.—EDAX positioning and results for processed sample at location 3 processed and unprocessed region. (a) SEM image of sample. (b) Spectroscopy analysis results; iron detected.

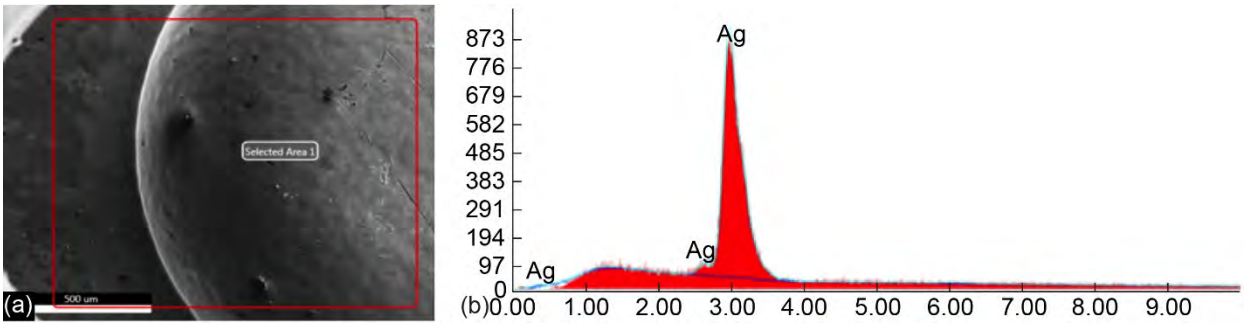

Figure 38.—EDAX positioning and results for processed sample at location 3 unprocessed region, position 5, 15 KeV. (a) SEM image of sample. (b) Spectroscopy analysis results; no iron detected.

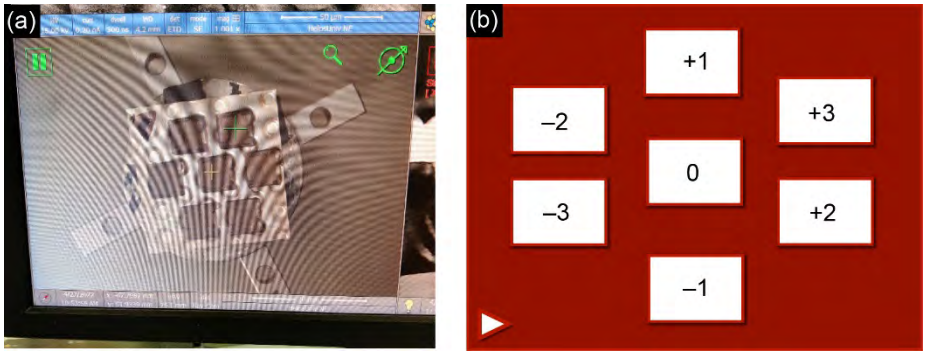

Figure 39.—EDAX area scans for processed sample at different locations relative to focus. (a) SEM image of sample. (b) Layout of EDAX sample scans at different locations (mm) relative to focus.

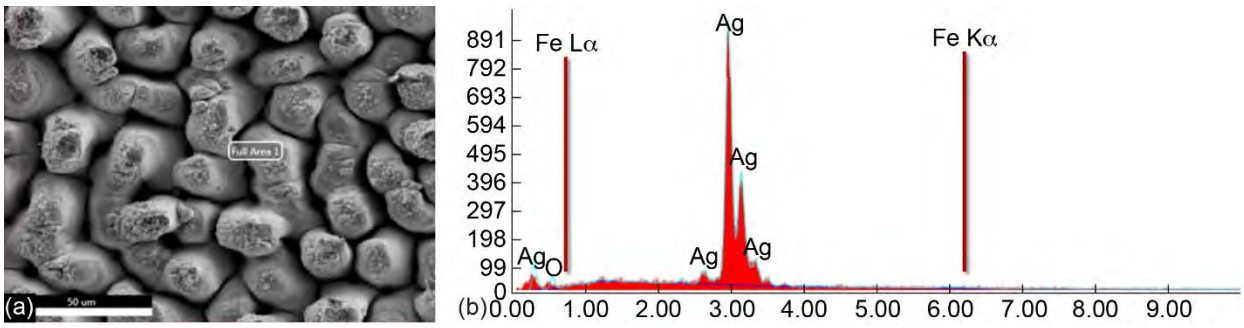

Figure 40.—EDAX area scans for processed sample at different locations relative to focus. (a) SEM image of sample. (b) Spectroscopy analysis results; no iron detected.

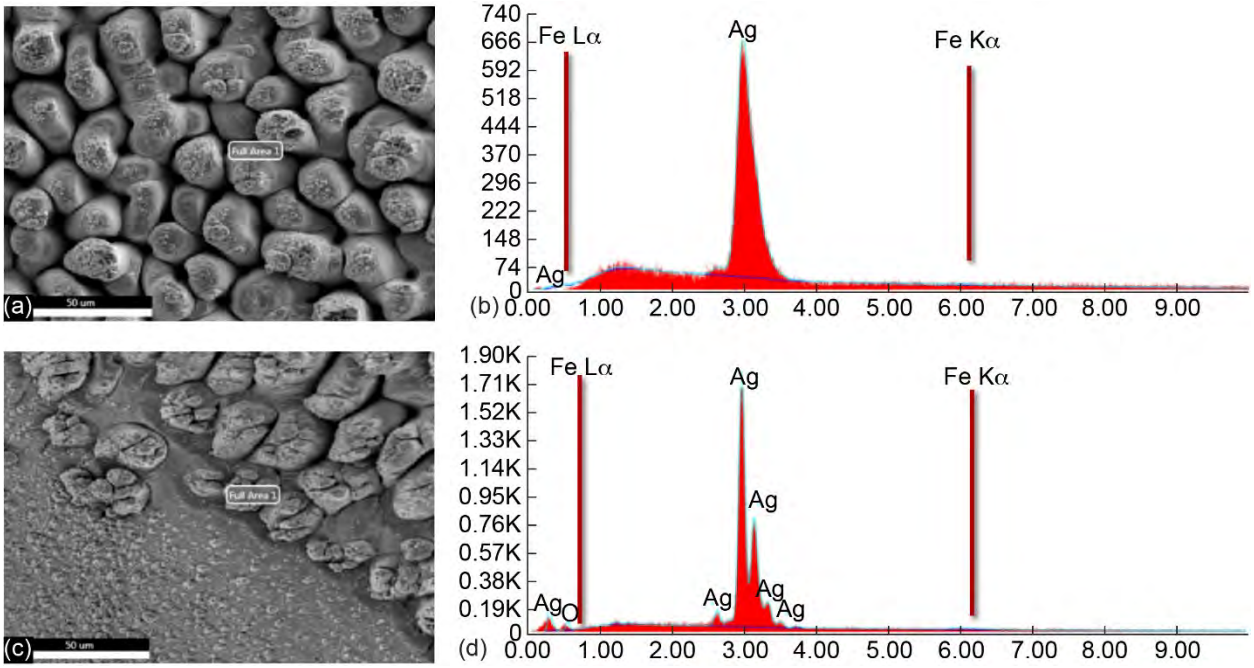

Figure 41.—EDAX area scans for processed samples compared at different locations relative to focus (±1 mm). (a) SEM image of sample at 1-mm focus. (b) Results for 1 mm; no iron detected. (c) SEM image of sample at –1 mm. (d) Results for –1 mm; no iron detected.

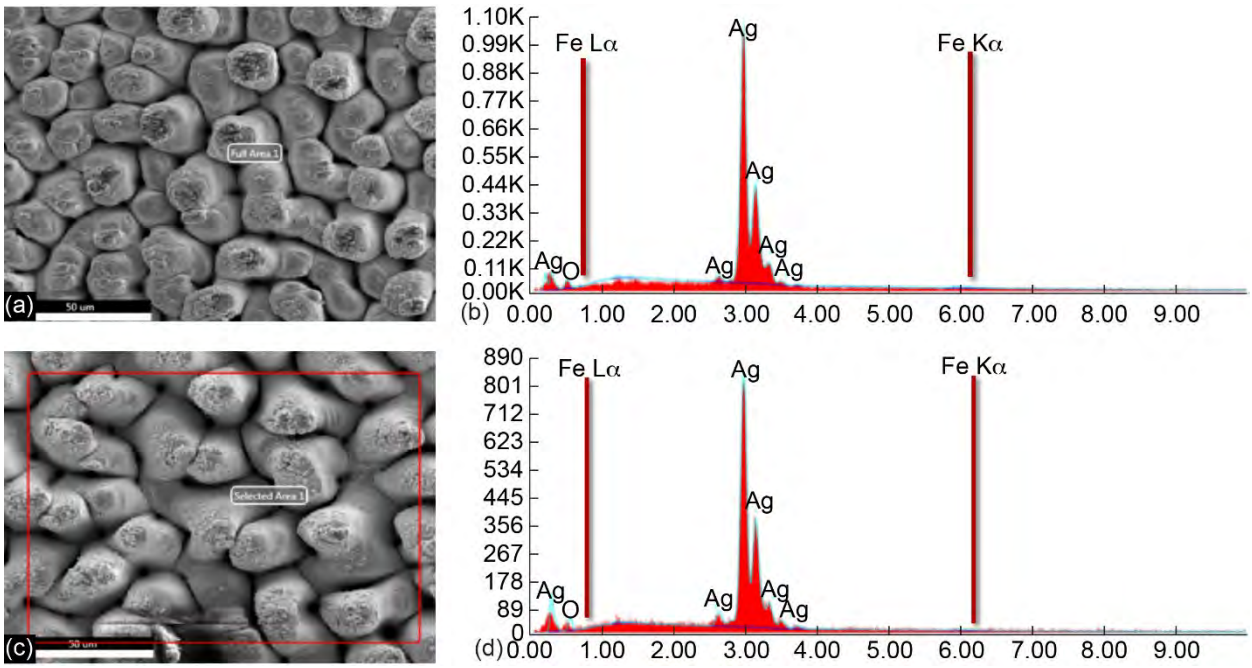

Figure 42.—EDAX area scans for processed samples compared at different locations relative to focus (±2 mm). (a) SEM image of sample at 2-mm focus. (b) Results for 2 mm; no iron detected. (c) SEM image of sample at –2 mm. (d) Results for –2 mm; no iron detected.

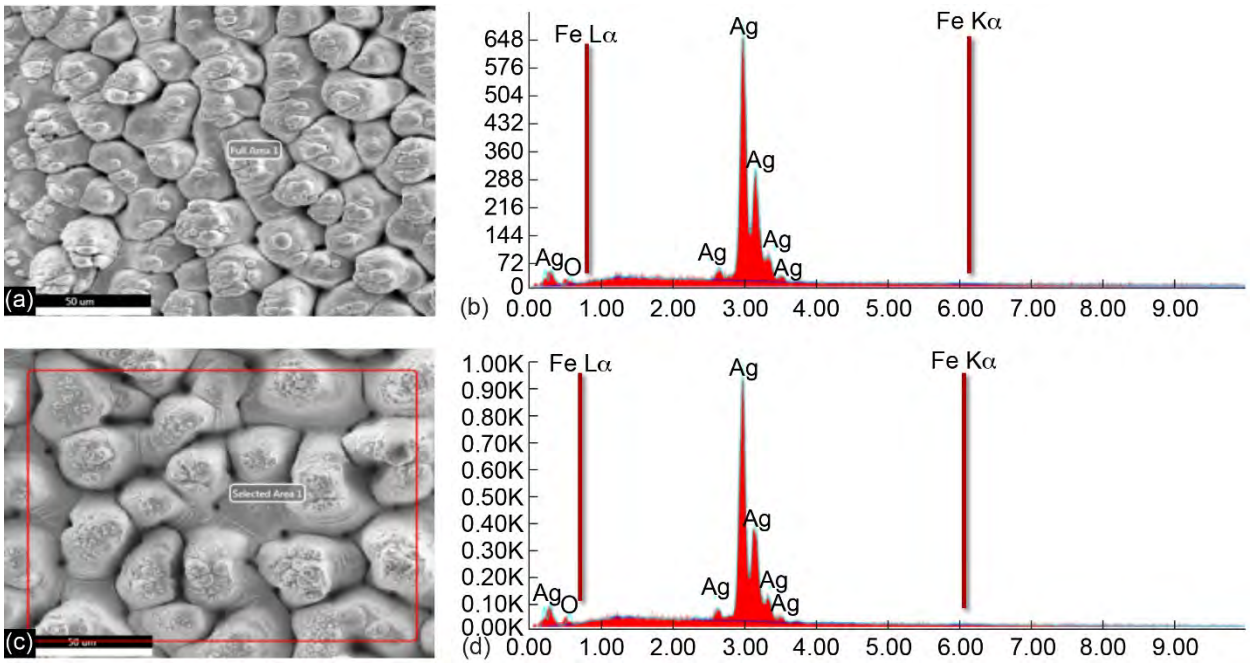

Figure 43.—EDAX area scans for processed samples compared at different locations relative to focus. (±3 mm). (a) SEM image of sample at 3-mm focus. (b) SEM image of sample at –3 mm. (c) Results for 3 mm; no iron detected. (d) Results for –3 mm; no iron detected.

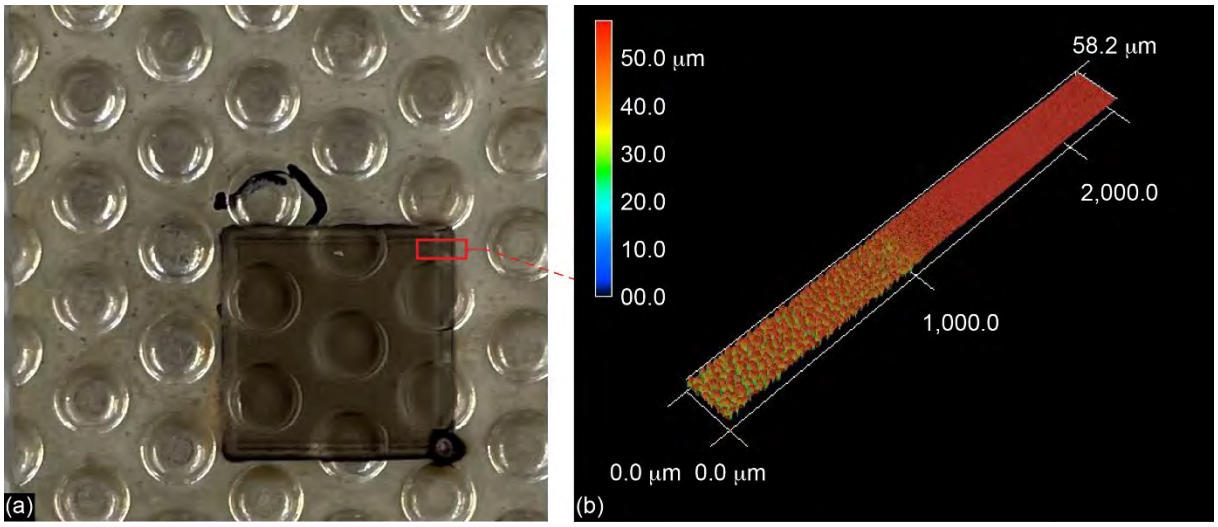

Figure 44.—Silver coating penetration by laser processing; maximum *d*, 56 µm. (a) Sample FLSP section used for analysis. (b) Results of analysis.

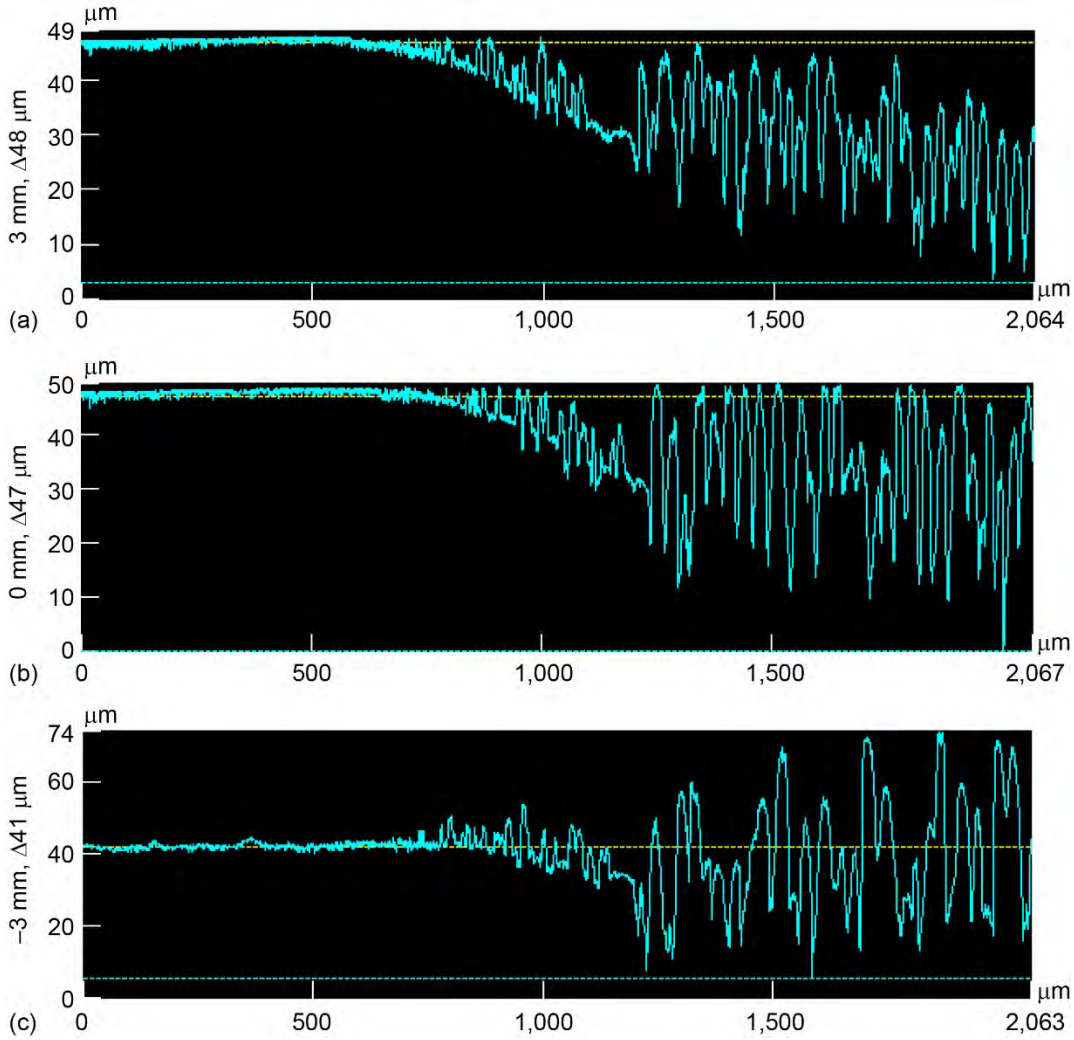

Figure 45.—Silver structure depth with varying laser parameters; maximum *d*, 48 µm. (a) 3 mm, 48 µm. (b) 0 mm, 47 µm. (c) –3 mm, 41 µm.

Based on the EDAX analysis of processed samples, there was no indication of exposed stainless steel, which was true for the as-received electroplated samples and the FLSP-processed samples. The analysis was conducted over a range of expected FLSP parameters, including variations in height that would occur on formed packets. The depth of the deepest valleys between structures relative to the original surface was up to 56.2 µm, which is less than the thickness of the 101.6-µm electroplated samples. This ensures a fully silver surface to aid in microbial tolerance for the system.

More EDAX imaging results can be found in Appendix B (Figure 78 to Figure 82).

4.5 Substrate Delamination and Cross-Sectional Analysis

This study found that LSCM and SEM data provide no evidence of plating delamination from the stainless steel substrate caused by FLSP, as illustrated in Figure 46 to Figure 48.

EDM cross-sectioning was used to analyze the coating of the stainless-steel-plus-silver interface post laser processing and found no indications of delamination (Figure 46). The same method was used to analyze the stainless-steel-plus-silver interface after FLSP (Figure 47). Both sides of the sample were processed. An unmodified boundary was identified between the silver and stainless-steel substrates. However, it was found that the wire EDM cross-sectioning was too destructive to measure FLSP penetration and was filling the valleys with melted materials.

There were no indications of delamination of the silver from the stainless steel after FLSP (Figure 48). There was access to the stainless steel at the corners of some dimples, causing potential mixing between the metals during EDM or excess materials being removed in the corners.

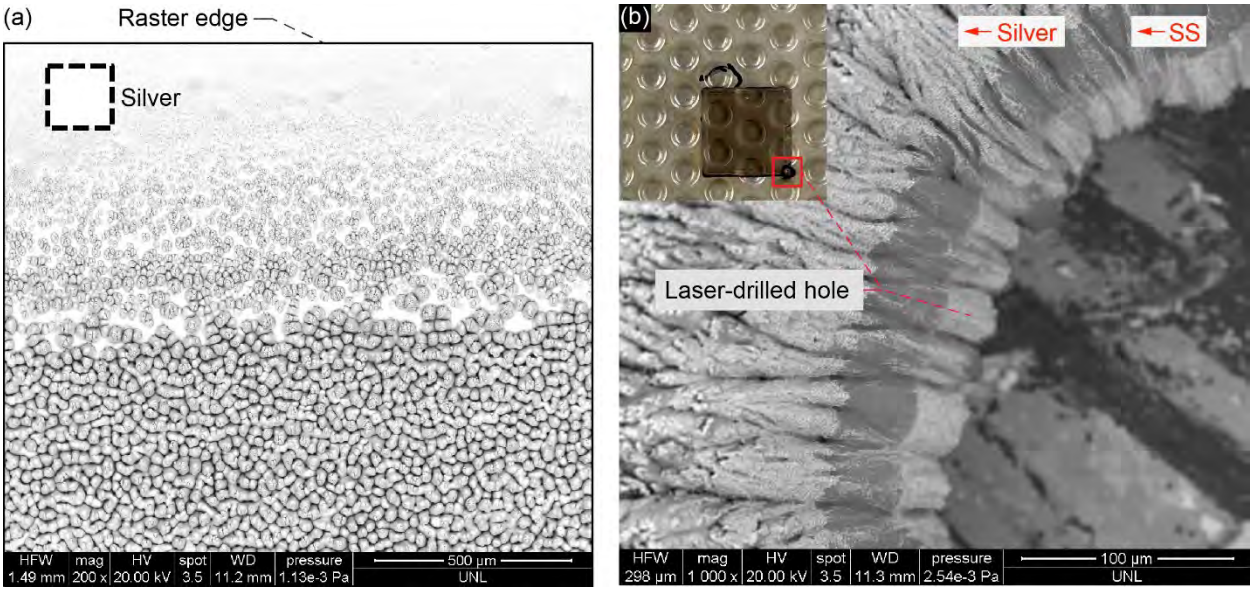

Figure 46.—Analysis of coating on stainless-steel-plus-silver (SS + silver) interface post laser processing; no indications of delamination. (a) Edge of laser raster path showing unprocessed silver and transition into processed mounds. (b) Intentionally drilled hole to examine SEM image of penetration depth of laser.

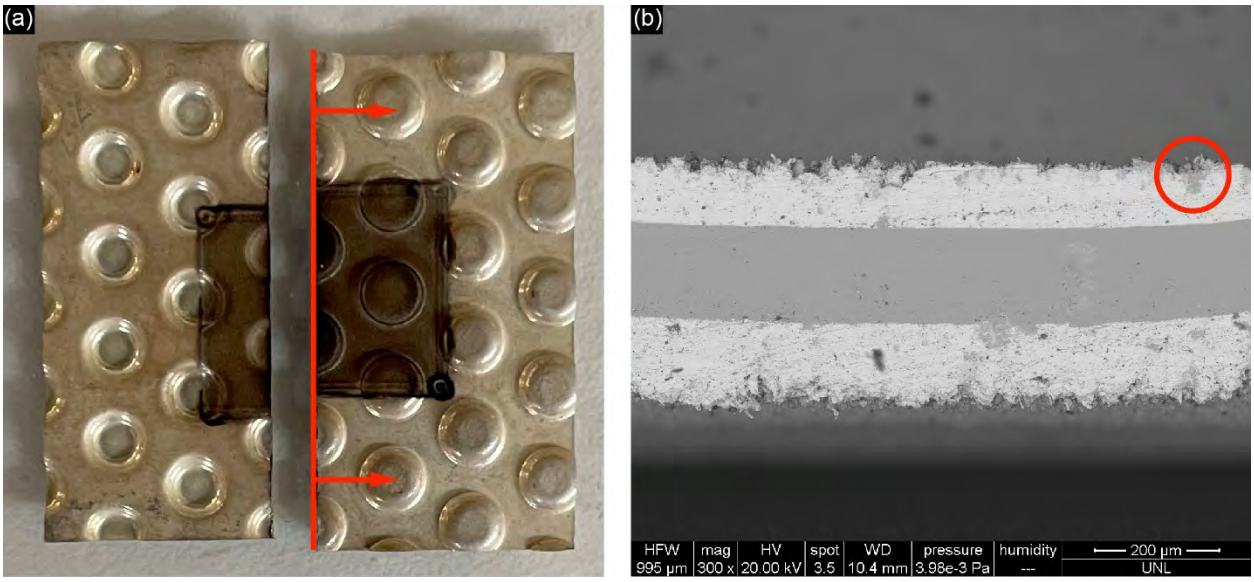

Figure 47.—EDM SEM-BSED cross-sectional analysis of laser-processed coated sample. (a) Sample FLSP section used for analysis. (b) SEM-BSED image of sample coupon.

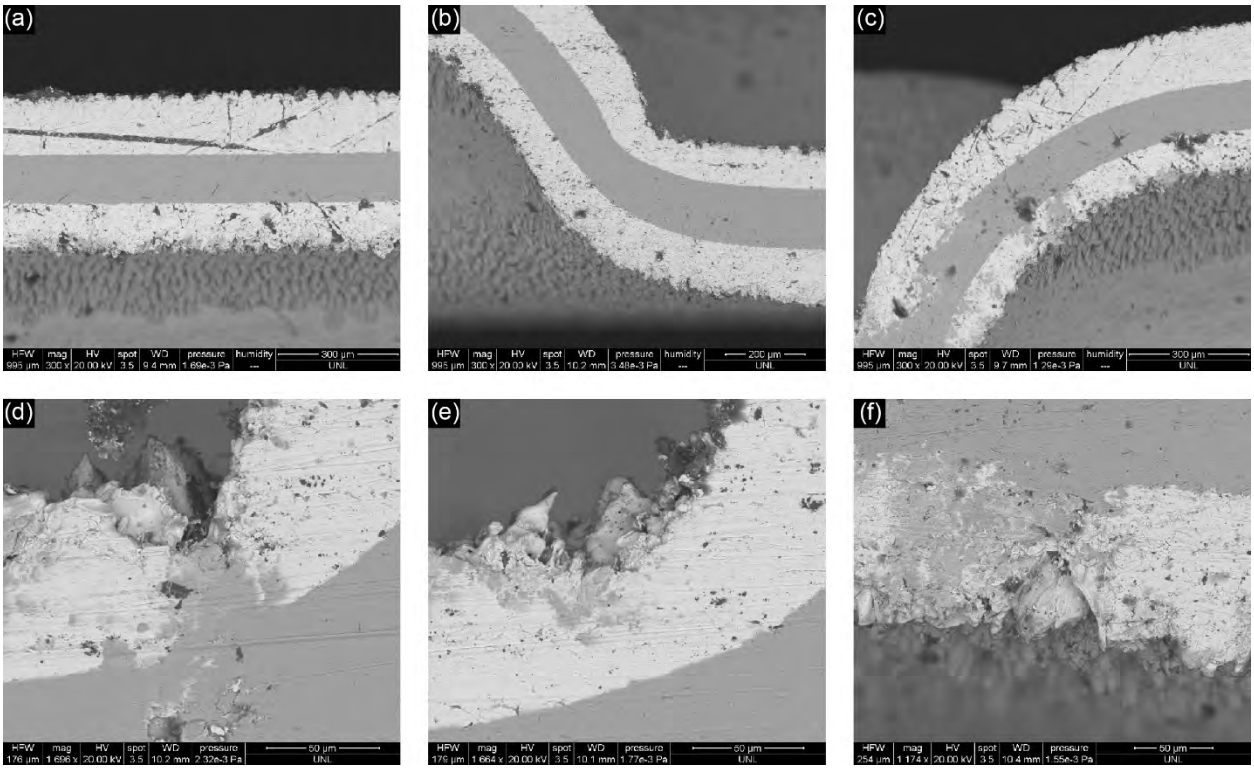

Figure 48.—EDM SEM-BSED cross-sectional analysis of laser-processed sample. (a) to (f) SEM-BSED images of sample coupon.

Cross-sectional sample analysis from the focused ion beam (Figure 49 to Figure 53) revealed a high porosity density in the peaks of the FLSO microstructures on the silver. It was estimated that this area of high-porosity materials was limited to the top ~20 μm of the mound. Although the porosity evident in Figure 51 to Figure 53 might be important for providing a large surface area for silver ion release, it was not accessible by the condensate.

Fully dense silver with large grains was located farther down in the sample (Figure 51); the structure of this silver was likely the same as that of the bulk material.

Following analysis of the full-scale LP-CHX packet (Figure 54 and Figure 55), it was determined that the processed packet had uniform FLSP features except for the >45° dimpled sidewalls, as discussed previously. The small feature variations in surface roughness (Table II) could be from variation in the height of the structure packet surface. Figure 56 shows a 3D view of negative (concave) dimples in the same sample at three different locations.

A full-scale electroplated packet was successfully created with uniform FLSP features analyzed by LSCM analysis. There were no discrepancies in the processing for the packet as compared to the silver packets in the 1/10th-scale unit project. The only difference was in the nonuniform processing of the dimple sidewalls that were greater than 45°, but this issue was expected. A permanent mounting fixture will need to be designed and manufactured to ensure consistent and efficient manufacturing of the full-scale CHX unit.

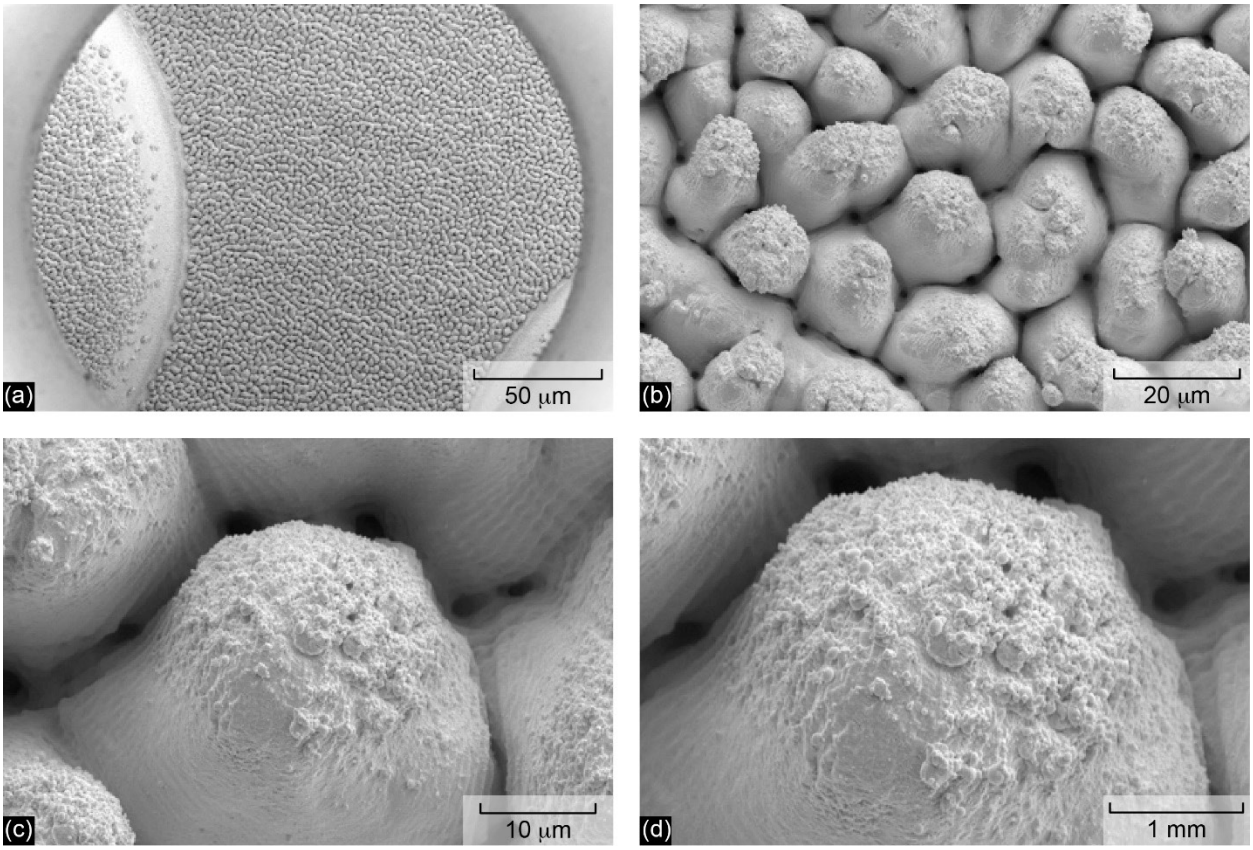

Figure 49.—Processed sample at location 3 before cross sectioning. (a) Top view. (b) to (d) Magnified views.

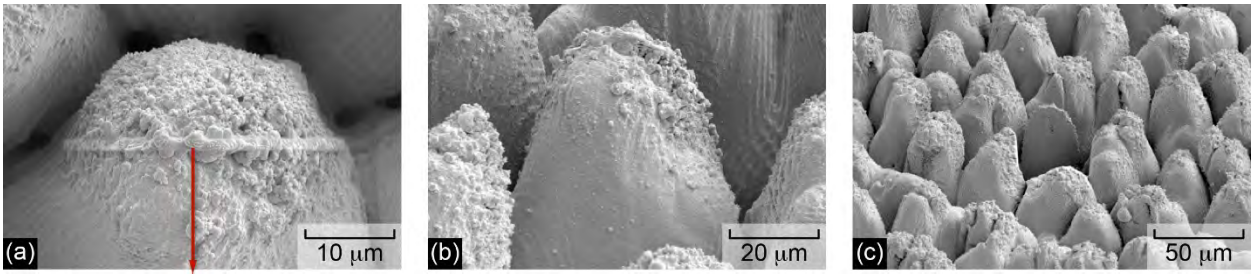

Figure 50.—Cross-sectioning of processed sample at location 3; imaged at 45° tilt. (a) Top view showing platinum deposited prior to cross sectioning. (b) Side view of platinum-deposit region prior to cross sectioning at lower magnification. (c) Cross-sectioning region.

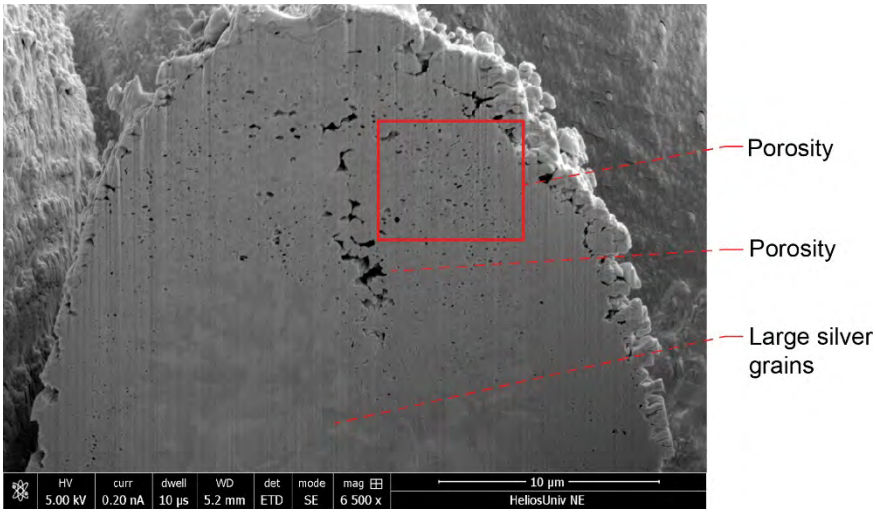

Figure 51.—Cross-sectioning of processed subsurface structure sample at location 3.

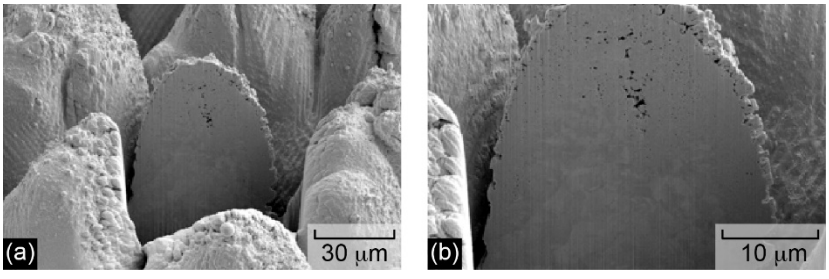

Figure 52.—Cross sectioning of processed subsurface structure sample at location 3. (a) At ×2500 magnification. (b) At ×5,000 magnification.

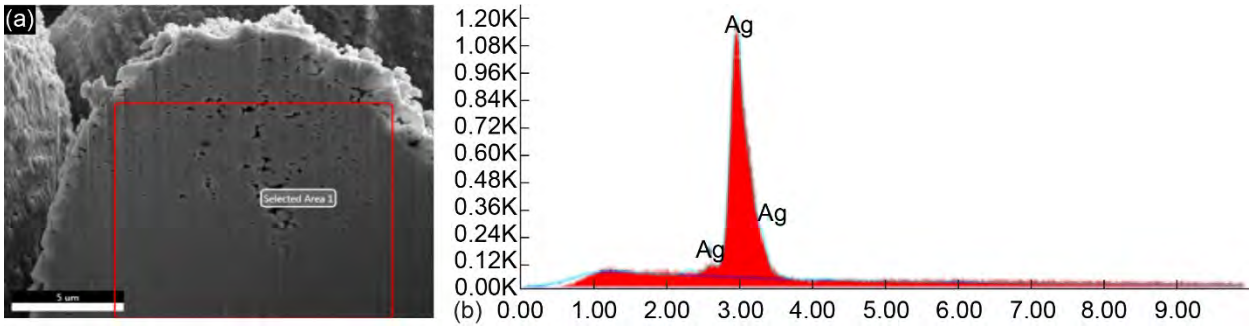

Figure 53.—EDAX results for processed region of sample at location 3, subsurface region, position 1, 15 KeV. (a) SEM image. (b) Spectroscopy analysis results; no iron detected.

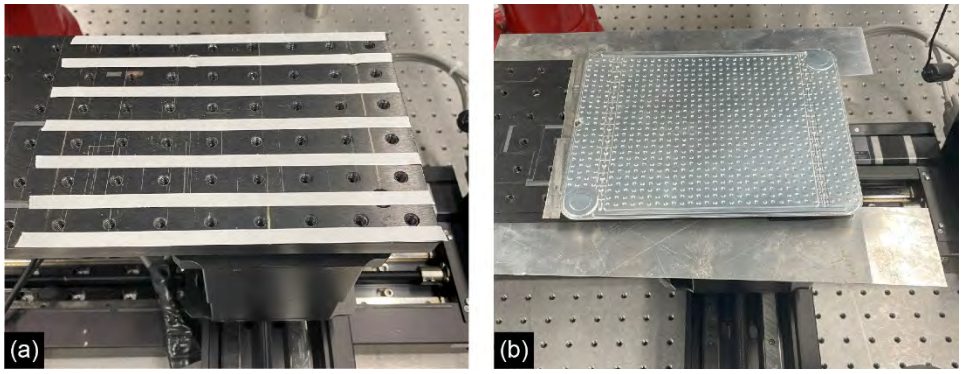

Figure 54.—Full-scale LP-CHX packet FLSP setup. (a) Sample stage for processing. (b) Sample secured onto stage.

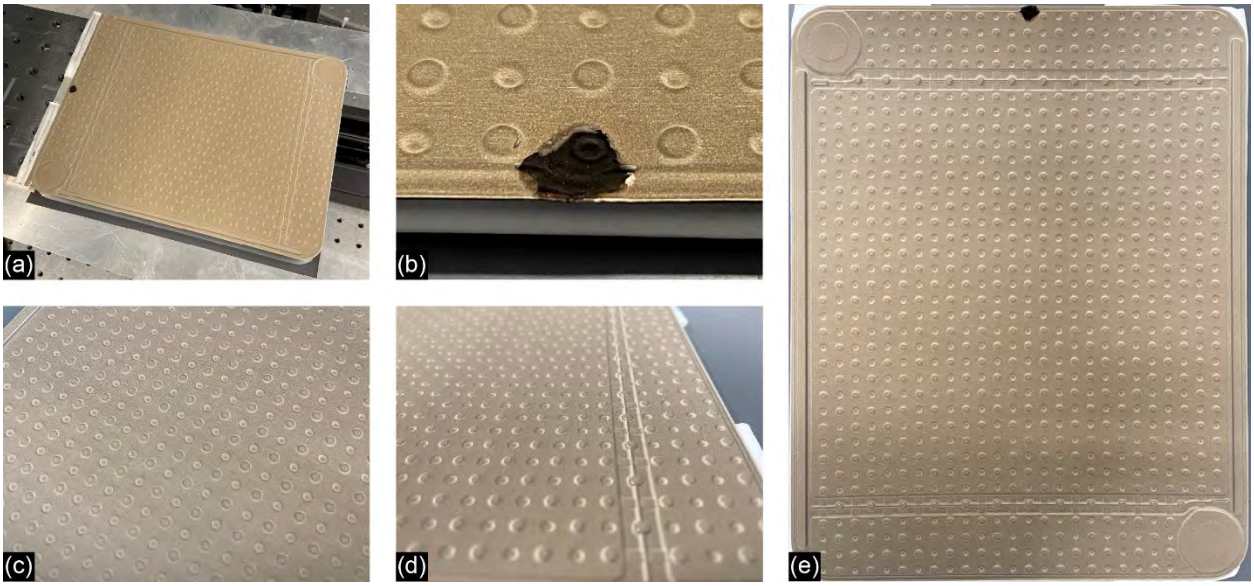

Figure 55.—Full-scale LP-CHX packet after electroplating. (a) Overall view. (b) Closeup of dimples. (c) Attachment point to electroplating rig. (d) Closeup of inlet line. (e) Full view of packet.

TABLE II.—ROUGHNESS ANALYSIS OF VARIOUS LASER-PROCESSED MOUNDS ON PACKET FEATURES SUCH AS DIMPLES AND RIDGES

Location	Feature	R_a, μm	R_z, μm	*SA/A*
1	Negative dimple	10.82±2.06	61.08±5.56	16.29±0.43
2	Negative dimple	11.93±1.40	68.33±5.74	11.29±0.46
3	Negative dimple	13.03±1.39	68.28±4.34	13.95±0.66
1	Positive dimple	10.22±0.91	57.11±3.06	15.14±0.93
2	Positive dimple	12.53±1.38	67.66±5.86	10.29±0.32
3	Positive dimple	12.35±0.88	63.34±3.86	11.61±0.27
4	Ridge	10.32±1.11	55.81±4.92	9.69±0.36

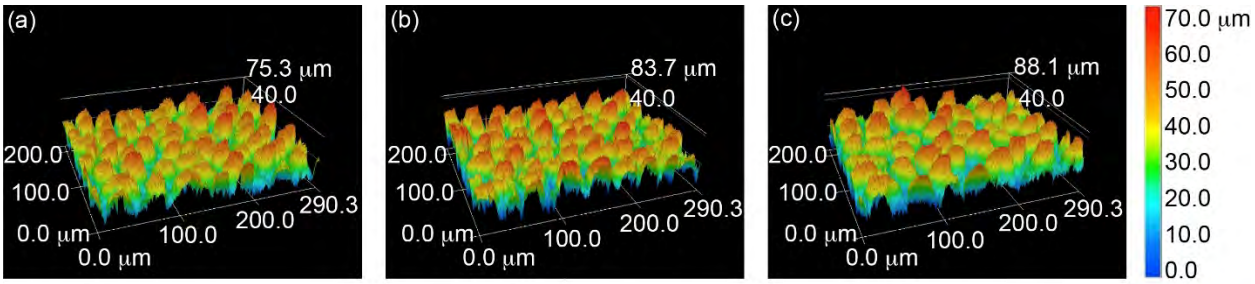

Figure 56.—3D view of negative dimples for one sample from same perspective at different locations. (a) Location 1. (b) Location 2. (c) Location 3.

(a) Sample	Processing rate, in^2/h	Time for full-scale CHX (150 packets), mo.
1/10th-scale unit	0.87	23.0
Full-scale electroplated packet	1.23	16.3

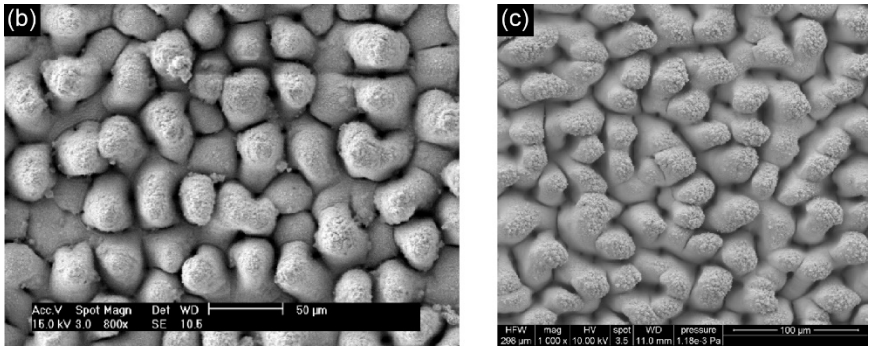

Figure 57.—Increased processing rates using the current laser at UNL. (a) Processing rate comparison. (b) Target sample, 1/10th-scale unit. (c) Project sample, full scale.

4.6 Scalability Study

During the processing of the full-scale packets, the processing rate had to be altered from the rate used on the 1/10th-scale unit. As seen in Figure 57, the rate was increased due to the optimization of laser parameters while simultaneously matching the structures on the 1/10th-scale unit. This increased rate was also used in the antimicrobial testing done by UNL.

UNL assisted in additional laser studies with more powerful lasers, using the Pulsed Laser Lab (PuLL) as part of the U.S. Army Space and Missile Defense Command (USASMDC) on the campus of University of Alabama-Huntsville (UAH). Two lasers were tested, a Coherent® (II-VI Delaware Inc.) Astrella laser at UNL and the Light Conversion® (Light Conversion, UAB) Pharos laser at PuLL, to determine which one would have the shortest processing time. The Astrella had an average power of 6 W, 5.4 mm/s raster velocity, 50 µm pitch, and a dual pulse at 120 ps. The dual pulses had crossed polarization and required a complex external setup to generate. The Pharos had an average power of 20 W, 40 mm/s raster velocity, 80 µm pitch, and a dual pulse at 200-ps pulse separation directly generated from the laser. The polarization of the dual pulses for this laser was matched. The comparison of spatial overlap in the two lasers can be seen in Figure 58.

The results showed a 5.29-times increase in average power and a 11.8-times increase in processing rate and predicted that the Astrella laser would take about 16.3 months for one full-scale CHX versus the Pharos, which would take 1.4 months. Examples of the produced structures can be seen in Figure 59.

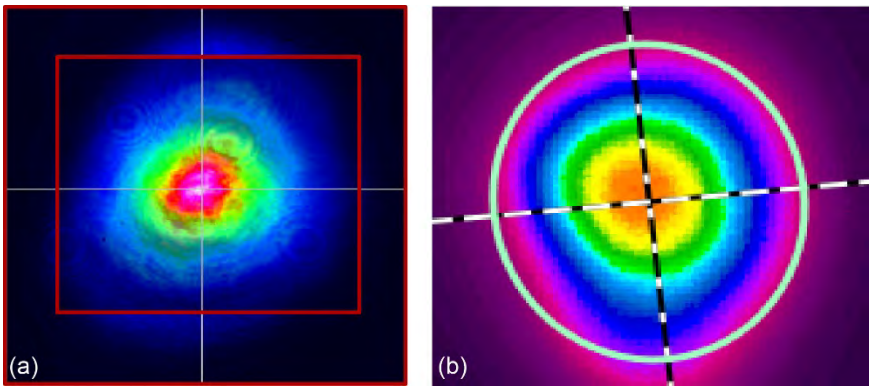

Figure 58.—Comparison of spatial overlap based on dual-pulse results.
(a) Astrella laser at UNL. (b) Pharos laser at UAH.

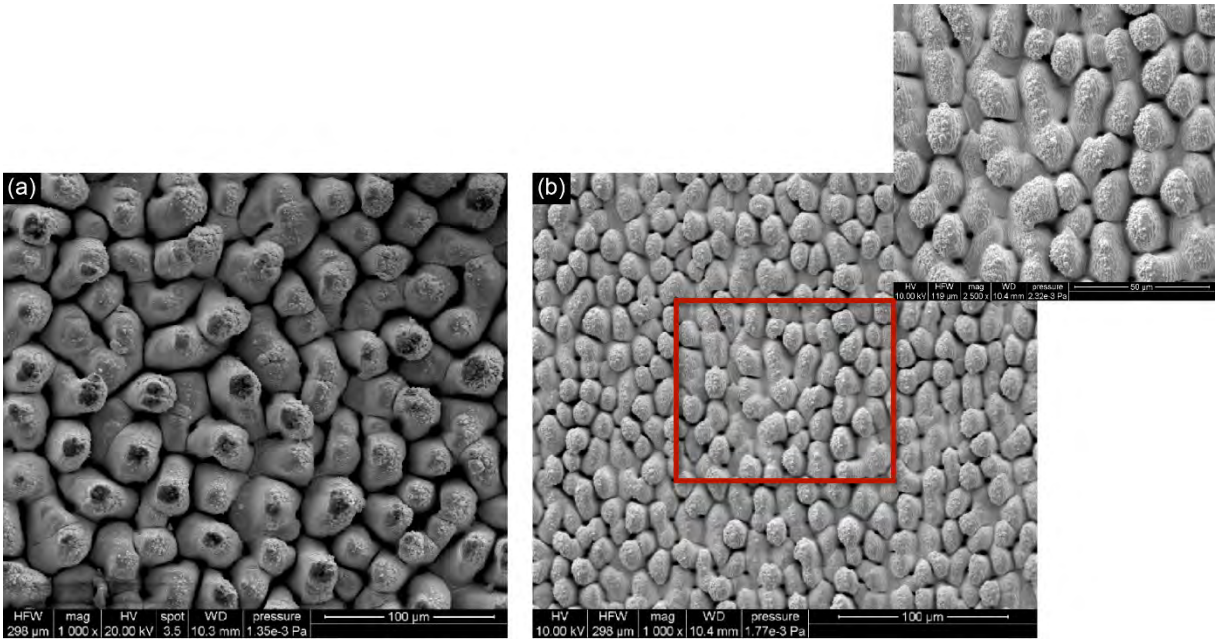

Figure 59.—Structures produced by Astrella and Pharos lasers. (a) Astrella (UNL). (b) Pharos (UAH).

A range of laser processing parameters such as velocity, pitch, and spot size were manipulated to verify that the processing rates previously targeted with the UNL laser can also be met with the UAH laser. This study is illustrated in Figure 60, showing evidence that spot size can be increased until the desired mound-type structures disappear, and velocity and pitch can be adjusted to maintain pulse count. The team tested the limits of the UAH laser to verify that identical surface structures could be created (Figure 61). From this data, it was found that high overlap of dual pulses is required for spot size optimization, and pitch can be used to compensate for stage velocity limitations. The greater overlap seen from the lasers' dual pulses enabled a larger parameter space and wider surface structure while maintaining the desired uniform structure.

Increasing laser power provided a direct increase in processing rate, though the expected processing rate with the UAH Pharos laser will eventually be limited due to the limited density supported by the silver material.

The testing completed by UNL demonstrated that FLSP works with the new class of high-repetition-rate ultrashort-pulse lasers that operate at a wavelength of 1,030 nm, unlike the older ones that operated at 800 nm. It is also important to note that the PuLL Pharos laser operates at a frequency of 10 kHz, whereas the UNL Astrella laser operates at 1 kHz. The testing showed that FLSP can be applied with very low energies, as low as 2 mJ. This is significant; before this project, the lowest successful pulse energy only reached 3.5 mJ. Optimizing the percentage of spatial overlap between each pulse allows for efficient use of available power. If an area is not overlapped, power could be wasted; at worst, it could be detrimental to structural formation. Due to the complex dual pulse setup at UNL, poor spatial overlap is more common between pulses; in contrast, the PuLL Pharos laser consistently produces perfectly aligned dual pulses.

The Pharos laser did not appear to be as sensitive to humidity as the current UNL laser; the humidity in the PuLL facility was greater than 50%.

UNL's analysis on plate thickness, imaging techniques, FLSP application, delamination probability, full-scale manufacturing, and potential scalability was the backbone to this project. The analysis provided enough evidence to support FLSP as a viable option as well as generating ideas to grow use cases for the technique. Utilizing previous ideas, projects, and techniques, UNL was able to supply Edare LLC, the company managing the electroplating process, with enough thickness data to find a compatible vendor to supply Johnson with proper samples to test microbially.

(a) Sample no. and description	Laser	Processing rate, in^2/hr	R_a, μm	R_z μm	*SA/A*	Time for full-scale CHX, mo.
1 – Best at UNL	Astrella	1.23	9.49	51.73	4.154	16.3[a]
2 – Similar structure to UNL at UAH	Pharos	2.96	9.48	53.48	4.400	5.5
3 – Fastest at UAH	Pharos	14.51	3.69	21.74	3.454	1.4

[a]UNL rate is based on time to process the full-scale packet.

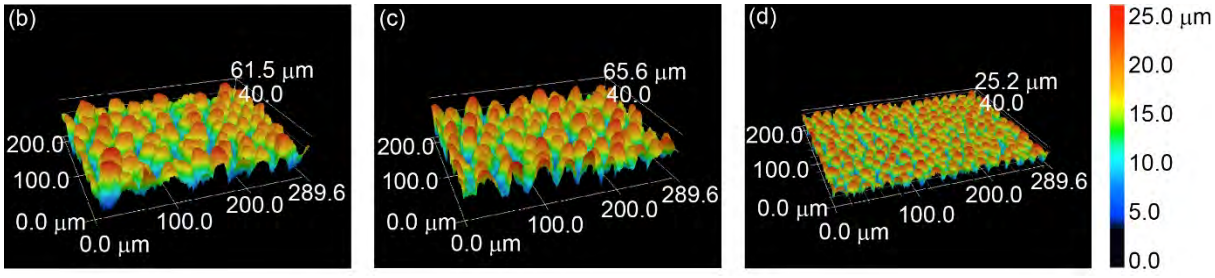

Figure 60.—LSCM analysis of "fast" FLSP on silver surfaces. (a) Laser processing rate comparison. (b) Sample 1 (best at UNL). (c) Sample 2 (similar structures to UNL at UAH). (d) Sample 3 (fastest at UAH).

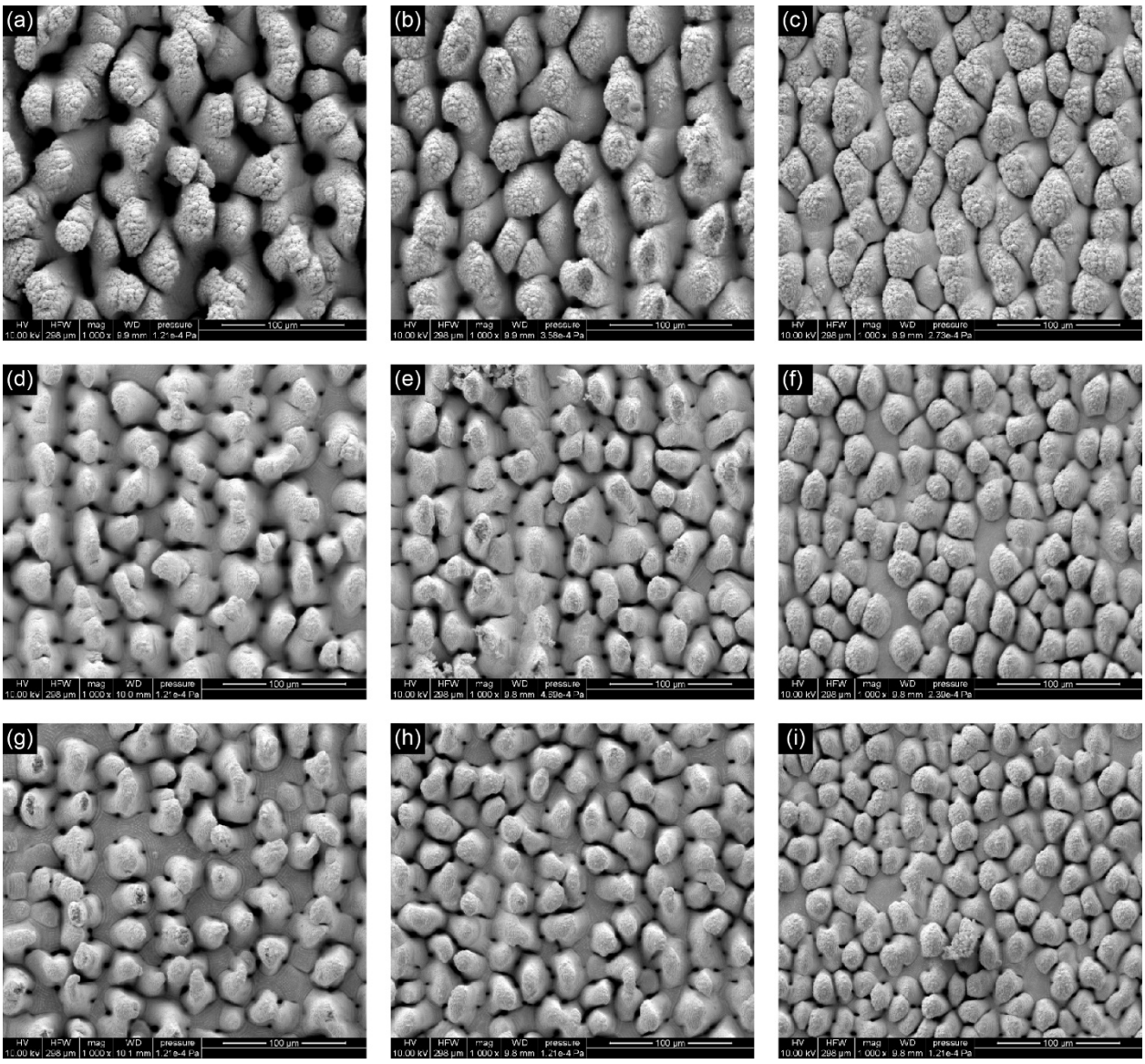

Figure 61.—Range of laser processing parameters on UAH Pharos laser. (a) to (c) 4 mm/s. (d) to (f) 20 mm/s. (g) to (i) 40 mm/s.

5.0 Work Performed at Edare, LLC Facility

The work completed by Edare revolved around the plating thickness and the capabilities of external manufacturers to produce necessary results. Edare worked with multiple vendors to investigate electroplating and determine its viability with silver on stainless steel. However, the studies delved much deeper than previous studies, comparing laser accuracy with cost efficiency to produce a detailed cost and schedule estimate for a fully scaled LP-CHX. Edare referenced ASTM B700-20, Standard Specification for Electrodeposited coatings of Silver for Engineering Use (Ref. 10), and ATSM B571-23, Standard Practice for Qualitative Adhesion Testing of Metallic Coatings (Ref. 11), to support the silver coating manufacturing plan.

5.1 Exploration of Additional Electroplating Vendors

Edare identified silver-plating vendors capable of producing the specified thickness and collected cost and fabrication details pertaining to full-scale production. They then fabricated sample coupons for additional microbial and full-scale packet production and provided vendor feedback on the results. Edare worked with NASA and UNL to evaluate variabilities in silver-plating processes as they pertain to the full-scale LP-CHX fabrication.

5.2 Potential Challenges

The quality of electroplated silver and stainless-steel packets highly depends on the tuning of various settings within the plating process. Although both vendors could produce high-quality parts, only one vendor expressed confidence in the ability to consistently produce viable packets. It was also found that each supplier missed the nominal thickness minimum by 0.0004 in. per side. It is predicted that Vendor 1 will be able to achieve successful plating quality after focusing on a single thickness rather than three separate thickness investigations.

6.0 Work Performed at Johnson Space Center Microbiology Laboratory

The microbial studies conducted by the Johnson microbiology laboratory investigated the current ISS CHX limitations, the compatibility of laser-processed silver, and the viability of the LP-CHX antimicrobial properties created through FLSP and other laser processes.

6.1 Preliminary Antimicrobial Sample Preparation by University of Nebraska-Lincoln

Before testing began at Johnson, preliminary testing preparation was completed at UNL using the previous technique of polished-wire EDM cross sectioning. The technique verified the electrodeposited silver thickness. The initial test matrix (Figure 62) assumes that there is an even disposition between the top and the bottom. The thickness of the electrodeposited silver was measured with a micrometer at the Edare facility (Figure 63); the reported thickness equaled the total measured value minus 0.006 in. (0.1524 mm). Averaging the measurements of the three locations, the top was 6.93% thicker than the bottom. Figure 64 shows the updated thickness matrix using averaged top-to-bottom distribution. Figure 65 shows the proposed antimicrobial sample selection; the samples sent to Johnson are shaded in yellow (thin samples, ~61 μm) and green (thicker samples, ~95 μm). The FLSP microstructures were measured to reach a depth of up to 56 μm. Figure 66 shows the manufacturing process of these antimicrobial samples. The created structures can be seen in Figure 67.

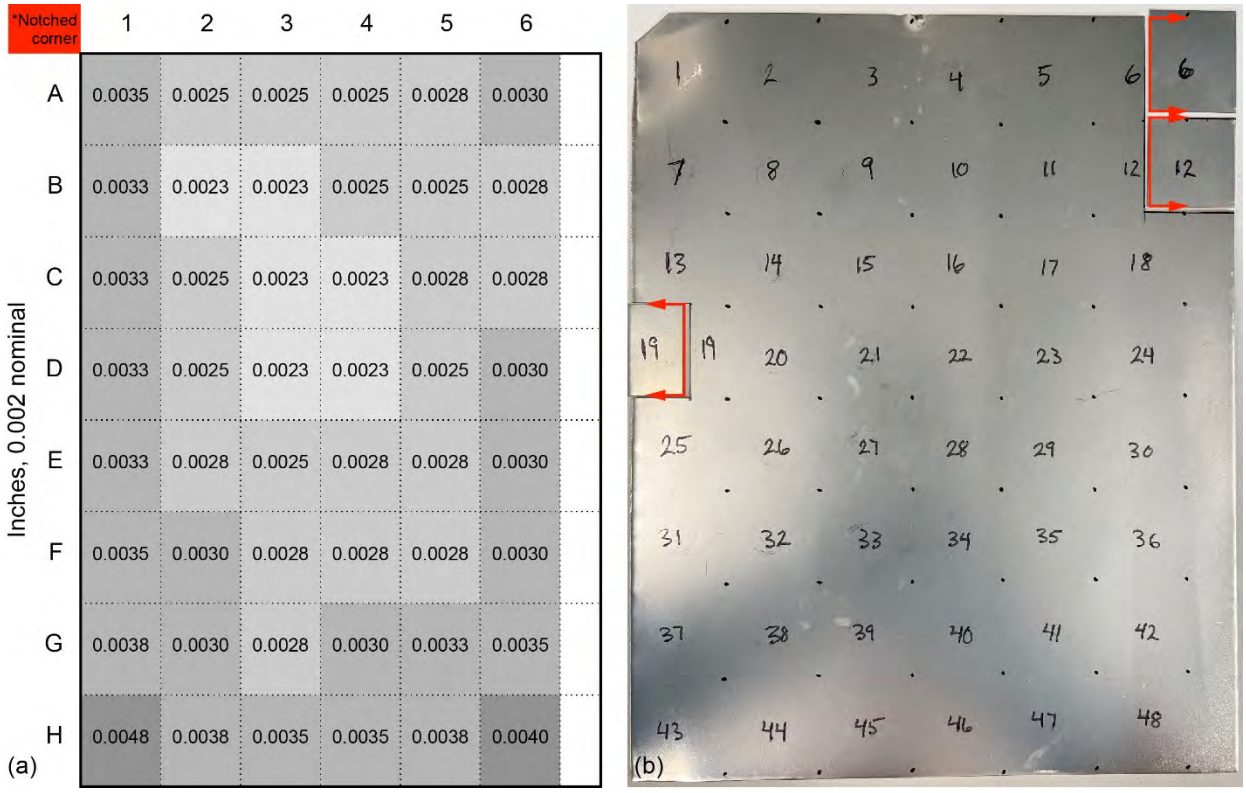

Figure 62.—Flat electroplated sheet (Ref. 9). (a) Test matrix. (b) Physical marked plate.

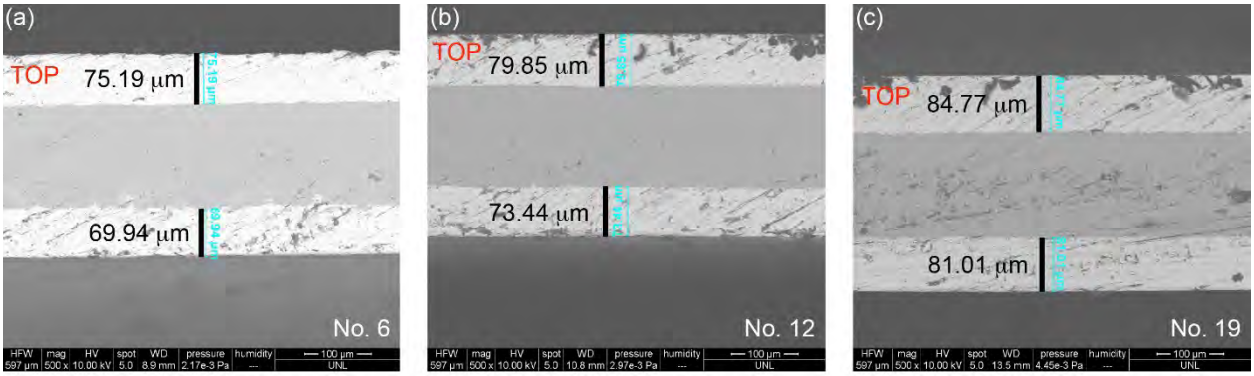

Top / bottom / total
Specified: 101.6 / 101.6 / 203.2 μm
Micrometer: 76.20 / 76.20 / 152.4 μm
SEM: 75.19 / 69.94 / 145.13 μm

Top / bottom / total
Specified:101.6 / 101.6 / 203.2 μm
Micrometer: 71.12 / 71.12 / 142.2 μm
SEM: 79.85 / 73.44 / 153.29 μm

Top / bottom / total
Specified:101.6 / 101.6 / 203.2 μm
Micrometer: 83.82 / 83.82 / 167.6 μm
SEM: 84.77 / 81.01 / 165.78 μm

Figure 63.—EDM cross sections of antimicrobial samples (Ref. 9). (a) Sample 6; top is 7.5% thicker than bottom. (b) Sample 12; top is 8.7% thicker than bottom. (c) Sample 19; top is 4.6% thicker than bottom.

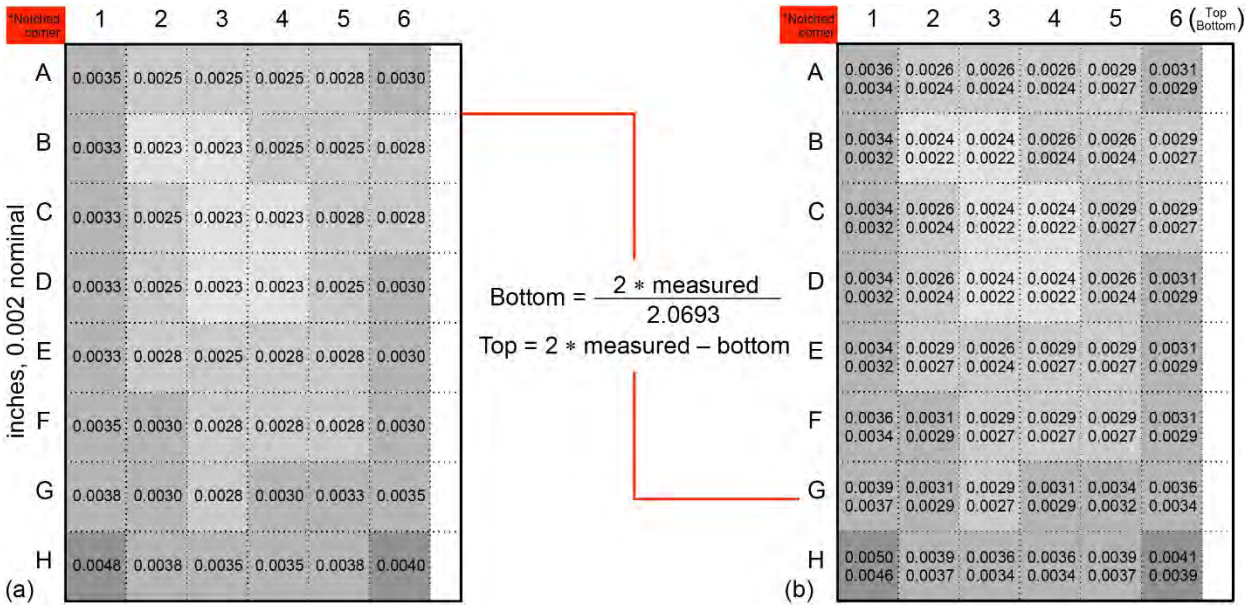

Figure 64.—Thickness matrix (Ref. 9); all values given in inches. (a) Original thickness matrix measurements. (b) Updated values, including top and bottom average distributions.

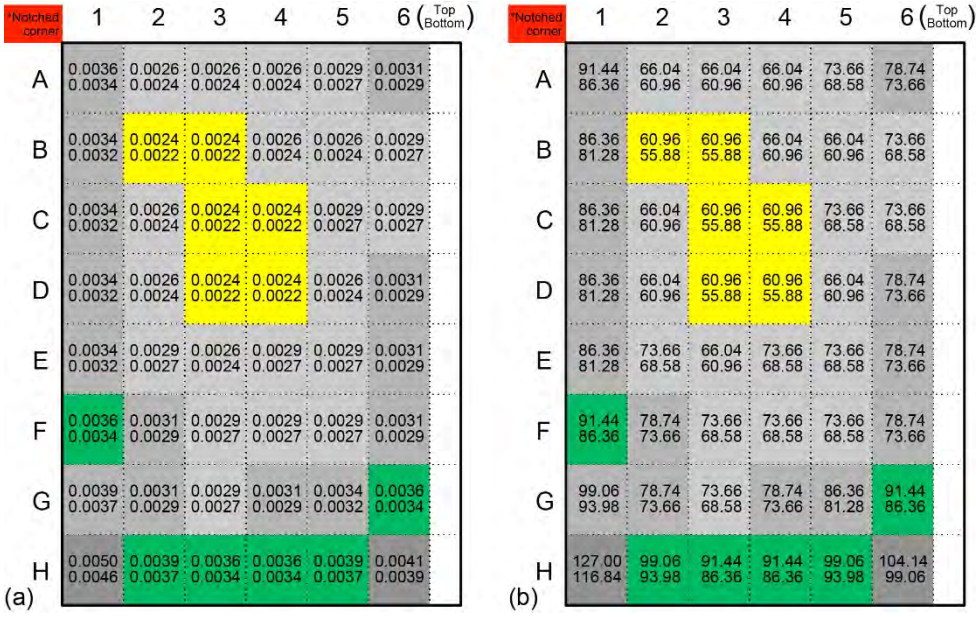

Figure 65.—Proposed antimicrobial sample selection; samples for Johnson shaded in yellow (thin, ~61 μm) and green (thick, ~95 μm). (Ref. 9). (a) Sample 1; values given in inches. (b) Sample 2; values given in μm.

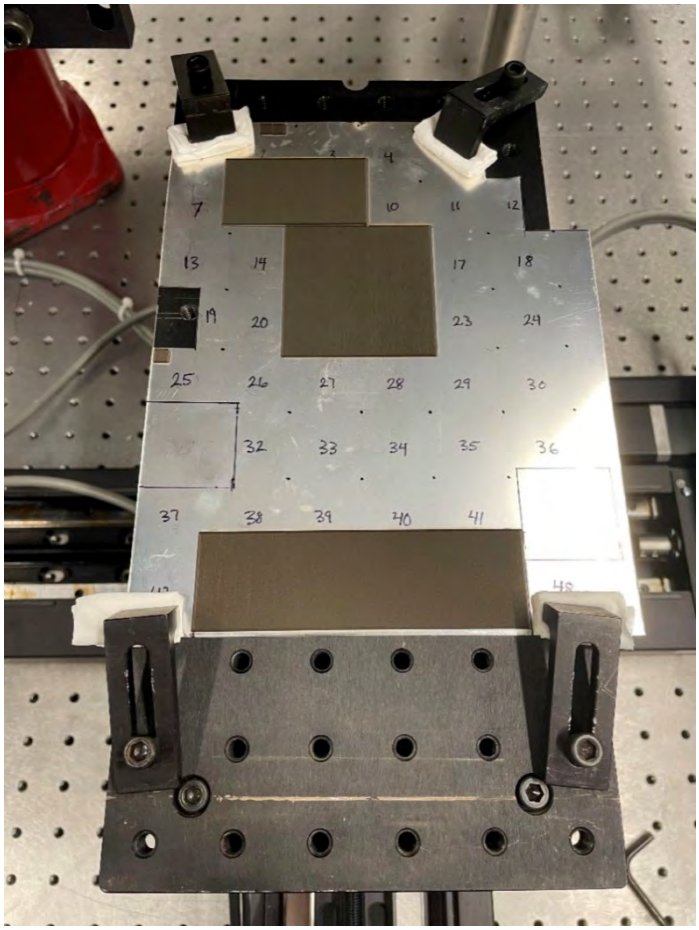

Figure 66.—Processing of antimicrobial sample (Ref. 9).

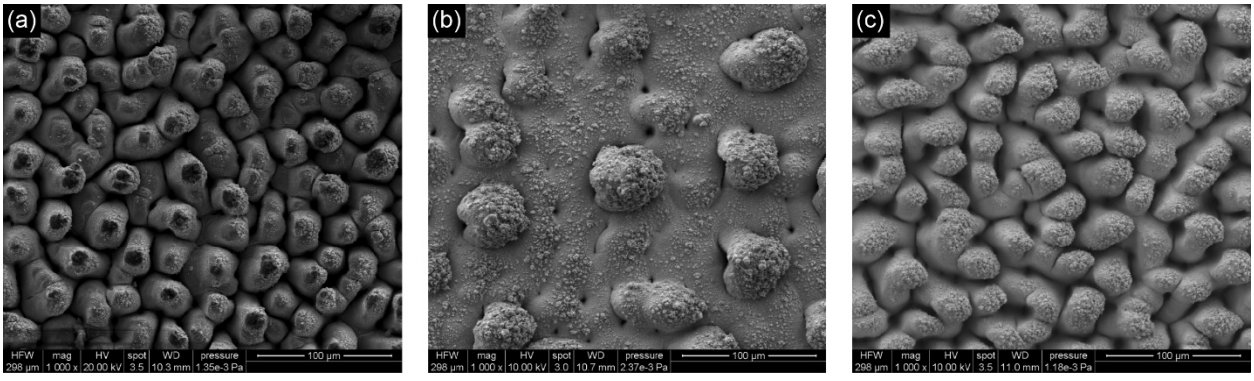

Figure 67.—Structure of antimicrobial samples (Ref. 9). (a) Previously used surface structuring. (b) Recent surface structuring with old parameters. (c) Surface structuring using stretched laser pulses.

From the antimicrobial sample tests conducted by UNL, it was determined that humidity can affect the laser processing workflow, increasing instability in the laser behaviors. The high humidity in the UNL laboratory affected the FLSP process, meaning there was a good chance the propagation or focusing behavior of the laser was changed. Stretching the laser pulses from 80 fs to 2.85 ps was implemented and appeared to counteract the negative effects from the humidity (Figure 67).

The full-scale packet was processed after the laboratory humidity decreased.

6.2 Johnson Space Center Microbiology Testing

Twelve samples were provided to NASA for antimicrobial studies with exceptional results, similar to those found under previous contracts. The Johnson microbiology laboratory used the following organisms for the 12 coupon tests shown in Figure 68:

- Staphylococcus epidermidis, commonly known as a staph infection; often found on human skin and mucous membranes
- Bacillus megaterium, known as sweet marjoram; an extremely large bacterium that is relatively easy to study and identify
- Sphingomonas paucimobilis, a bacterium found in soil and water that could potentially cause infections in immunocompromised individuals
- Aspergillus brasiliensis, a fungus that produces black spores and is a common food contaminant

These organisms represent a wide variety of potential hazards found on the ISS and provided ample evidence to support the implementation of the LP-CHX packets.

6.2.1 Microbial Testing Preparation

The samples provided by UNL were prepared for microbial testing in the Johnson microbiology laboratory. The purity of each sample was verified by using two mechanical analyzers, the 3500 Genetic Analyzer (Thermo Fisher Scientific Inc.) and the VITEK® 2 COMPACT Microbiological Analyzer (bioMérieux, Inc.). Researchers identified the proper bacterium to test, calculated the organism's overnight concentration (Figure 69), and sterilized all materials that would be used for testing.

Johnson then conducted testing on the consortium (Figure 70) by diluting the bacterial concentration down to ~10^5 colony-forming units, taking count of the filamentous fungus spores; the spore concentration was ~10^4. Using the data collected, a total consortium volume of 10 mL was generated at these bacterial and fungal concentrations.

Figure 68.—All 12 coupon samples arriving at Johnson (Ref. 12).

Figure 69.—Overnight bacterium concentrations (Ref. 12).

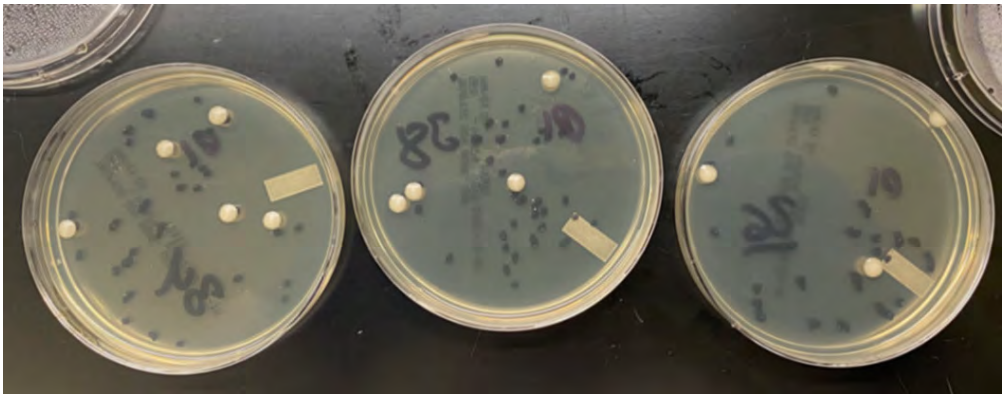

Figure 70.—Samples from consortium testing (Ref. 12).

Figure 71.—Closeup of two coupons configured for microbial testing (Ref. 12).

6.2.2 Microbial Testing Procedure

Inoculation of the 12 microbial organisms was then conducted on one side of each sample, allotting 2 hr for microbial adherence before giving the samples nutrients for overnight growth. After the allotted 24 hr for growth, the samples were put through sonication, a type of sound energy application, and vortex mixing before being plated. Each of the 12 coupons was configured within its own petri dish, as seen in Figure 71 and Figure 72. The trials were performed in biological and technical triplicates (n = 3), a common technical practice to verify trial results.

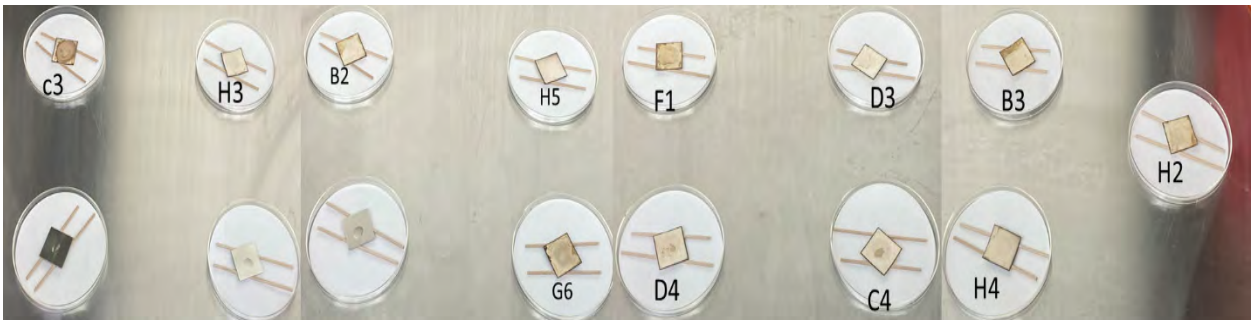

Figure 72.—All 12 coupon samples undergoing microbial testing (Ref. 12).

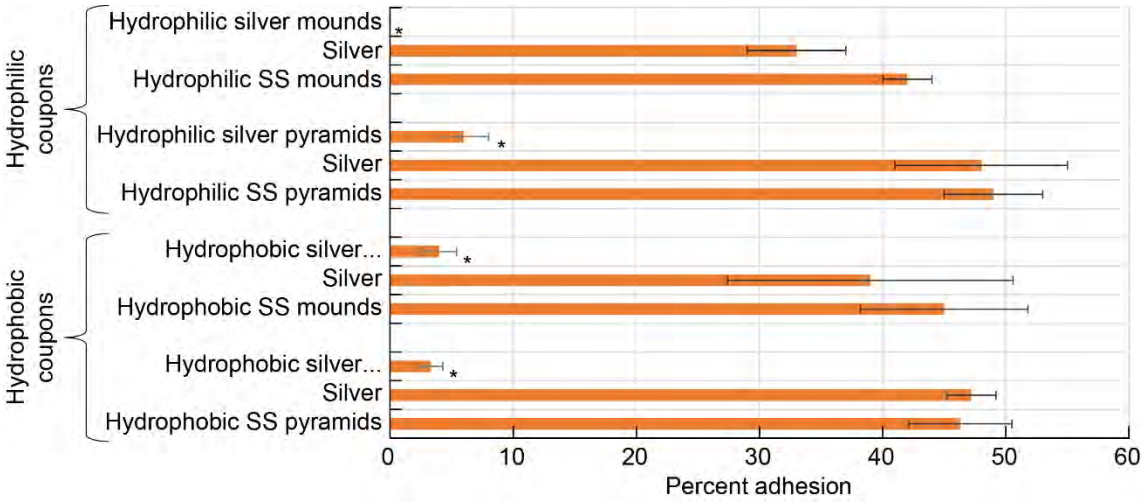

Figure 73.—Microbial study conducted at Johnson comparing various laser processing treatments on mound and pyramid surface structures (Ref. 12).

6.2.3 Microbial Testing Results

Before this project, the initial studies conducted found that laser processing treatment of antimicrobial surfaces, such as most silver substrates, can achieve great reduction in microbial growth with no visible property or structural degradation over time. Prior to exploring LP-CHX manufacturing, various laser processing treatments were implemented on various surfaces to study bacterial adhesion (Figure 73) (Ref. 12). It was found that, out of the 12 coupons tested, the sample coupons with the hydrophilic stainless-steel pyramids and hydrophilic silver had the highest percentage of bacterial adhesion, whereas the hydrophilic silver mounds had 0% bacterial adhesion, leading to further investigation in this project.

The results shown in Table III present the findings from the original microbial sample testing in Figure 72 and are further demonstrated with the graphs in Figure 74 and Figure 75. The thickness classifications in Table III refer to the thickness of that specific sample section, with “thin” being ~61 µm and “thick” being ~95 µm (Figure 64). As shown in Figure 74, the three unprocessed stainless steel control trials showed 100% microbial recovery; in contrast, the 12 hydrophobic silver mound samples in Figure 75 had 0% microbial recovery, meaning there was no adhesion to the surface.

TABLE III.—RESULTS FOR SAMPLES SHOWN IN FIGURE 72 (REF. 12)

Name	Thickness[a]	Accelerated[b]
B2	Thin	No
B3	Thin	No
C3	Thin	No
C4	Thin	Yes
D3	Thin	Yes
D4	Thin	Yes
F1	Thick	No
G6	Thick	No
H2	Thick	No
H3	Thick	Yes
H4	Thick	Yes
H5	Thick	Yes

[a]Thin, ~61 µm; thick, ~95 µm.
[b]Equivalent to 6 mos. of testing.

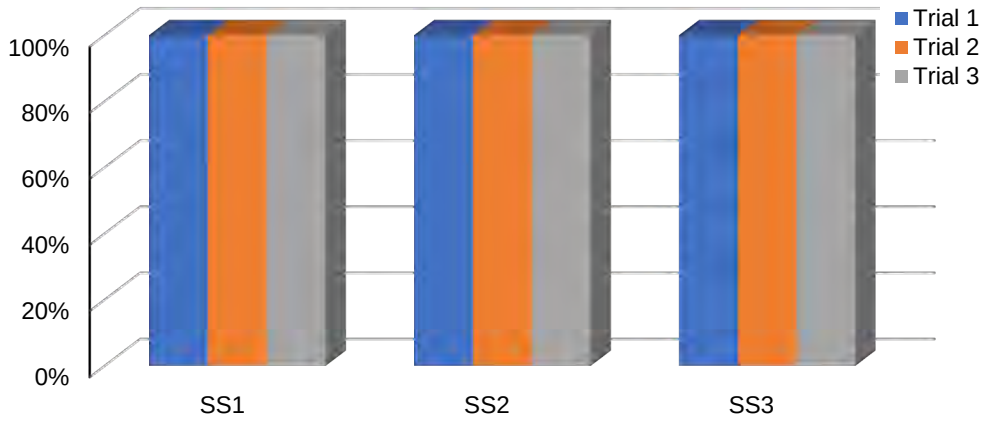

Figure 74.—Microbial recovery on stainless steel structures. (Ref. 12).

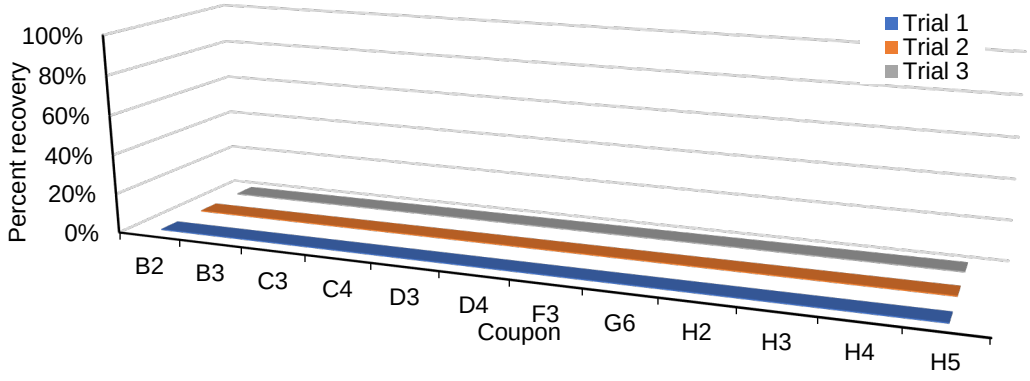

Figure 75.—Microbial recovery on silver mound structure sample coupons.

Through this testing application at Johnson, minimal growth of bacterial and fungal organisms was observed. The results are reproducible, establishing the LP-CHX as a viable alternative for ISS and other spacecraft use when microbial control is needed.

7.0 Additional Microbial Study Results

Initial trials first demonstrating the properties of femtosecond-laser-processed samples for life support purposes were performed by Johnson in 2021. Scott Hansen and others set out to build a controlled environment to test how the wettability of the CHX surfaces is affected when exposed to siloxanes found on the ISS. The trials monitored the change in contact angle and examined the change in surface properties over time to determine how these packets might change in a space vehicle environment. The test focused only on stainless steel and found, after analyzing flow rates, surface pattern, and siloxane injection occurrence, that the samples with mound structures started and ended more hydrophobic than the pyramid-patterned samples. In fact, all samples eventually turned hydrophobic regardless of their initial wettability properties, making the original hydrophilic designs unfeasible (Ref. 13).

The LP-CHX design was originally based on wettability results and sought to expand upon those results by using silver as the substrate. Current spaceflight heritage systems use technology akin to space shuttle humidity separators to remove the condensed water. In parallel to this LP-CHX work, other outside companies are working to create new concepts for water separator technology that can pair with LP-CHX systems. The most promising technologies are air separators that are implemented downstream of the LP-CHX unit for integration in the larger ECLSS system; these separators offer advantages in water recovery over current ISS systems (Ref. 14).

8.0 Conclusions

The Laser-Processed Condensing Heat Exchanger (LP-CHX) project set out to explore the viability of electroplating processes on stainless steel and silver packets in CHX manufacturing, and the LP-CHX has proven to be a promising alternative to the current chemically coated condensing heat exchanger in place on the International Space Station. Implementation of LP-CHX technology would not only eliminate the need for a chemical coating entirely but could potentially cut manufacturing time by 18 months, save over $1 million in overall costs, and greatly reduce resources use. Moreover, the LP-CHX accomplishes the key parameter of a 4.192-kW output and falls within the acceptable range for a targeted flight pressure drop of 248.84 Pa. Highly favored by NASA’s Habitation Systems, Advanced Exploration Systems, and the Environmental Control and Life Support Systems (ECLSS) Systems Capability Leadership Team, the LP-CHX can be produced at full-scale sizing on a timeline akin to those associated with existing hardware in use, making implementation of this innovation extremely feasible for integration in upcoming long-duration spaceflight, such as on a mission to Mars.

Appendix A.—Nomenclature

A.1 Acronyms

3D	three-dimensional
BSED	backscattered electron detection
CEFS	Center for Electro-Optics and Functionalized Surfaces
CFD	computational fluid dynamics
CHX	condensing heat exchanger
DMSD	dimethylsilanediol ($C_2H_8O_2Si$)
ECLSS	Environmental Control and Life Support Systems
EDM	electrical discharge machining
EDAX	energy-dispersive analysis via x-ray
FLSP	femtosecond laser surface processing
HX	heat exchanger
ISS	International Space Station
KPI	key performance indicator
LP	laser processed
LP-CHX	laser-processed condensing heat exchanger
LSCM	laser scanning confocal microscope/microscopy
PuLL	Pulsed Laser Lab
SCLT	Systems Capability Leadership Team
SEM	scanning electron microscope/microscopy
SS	stainless steel
SST	shear stress transport
TRL	Technology Readiness Level
UAH	University of Alabama-Huntsville
UNL	University of Nebraska-Lincoln
USASMDC	United States Army Space and Missile Defense Command
WD	working distance
WPA	Water Processor Assembly
XCT	x-ray computed tomography

A.2 Symbols

A	area, m^2
C_p	specific heat capacity at constant pressure, J/kg/K
D	diameter, m
D_h	hydraulic diameter, m
d	depth of penetration, μm
dz	spacing of cut plane
f	frequency, kHz
f_P	pitch, μm
h	heat transfer coefficient, $W/m^2/K$

$\bar{h}$	average heat transfer coefficient, W/m^2/K
k	thermal conductivity, W/m/K
L	length, m
m_{cell}	mass in cell, kg
m_{cond}	mass of condensate, kg
m_{tot}	total mass, kg
m_v	mass of gas vapor, kg
N	normal vector to wall, m
Nu	Nusselt number
$\overline{\text{Nu}}$	average Nusselt number
P	perimeter, m
P_o	power, W
P_p	pressure, Pa
p_{cell}	pressure in cell, kPA/kg
Pr	Prandtl number
q''	heat flux, W/m^2
q_{cell}	heat transfer in cell, J/kg
q_{cond}	heat transfer of condensate, J/kg
q_{conv}	convective heat transfer, J/kg
q_{wall}	wall heat transfer, J/kg
R	processing rate, in^2/hr
R_a	surface roughness average, µm
R_z	max surface roughness height average, µm
Re	Reynolds number
Re_x	Reynolds number, x-direction
RH_{cell}	relative humidity in cell, %
SA	surface area
T	temperature
T_c	cell temperature, K
T_g	gas temperature, K
T_i	temperature at inlet, K
T_{ref}	reference temperature, K
T_w	wall temperature, K
t	pulse separation/dual pulse, ps
U	velocity vector, m/s
u	x-direction velocity, m/s
V	volume, mL
V_r	raster velocity, mm/s
µ	dynamic viscosity, Pa·s
ρ	density, kg/m^3
ω	specific rate of kinetic energy dissipation, s^{-1}

Appendix B.—Additional Figures

Figure 76 shows the Python postprocessing script, which determines the local Nusselt number at each plane before performing trapezoidal integration across the domain to determine the average Nu number for the condensing heat exchanger (CHX).

Figure 77 shows the condensation and heat rate spreadsheet. Once the Nu number is updated in this sheet, the macro can be run, results can be collected, and the new pressure results from the Ansys® Fluent® software (Ansys, Inc.) can be analyzed (Ref. 2).

Figure 78 to Figure 82 show EDAX positioning and results for processed samples for various location 3 positions.

```
    Created By: Ezra McNichols 04132022

    Edits:
        Kyle Monaghan 04132022 -
    """

    import numpy as np
    import matplotlib.pyplot as plt
    from pandas import *

    # Read in the data from ANSYS. Columns are assumed to be arranged by: z, q, Tm
    data = read_csv("Ansys_dimpled_flow_v2.csv",header=None,skiprows=0)
    data.columns = ['z','q','Tm', 'Tw']

    # These values are geometric and material properties for the calculations. Make sure these match the ANSYS model.
    Tw = 500        # Constant wall temperature
    k = 0.0242      # Thermal conductivity of the fluid
    D = 0.001889193       # Hydraulic diameter
    L = 0.2032      # Overall length
    dz = 0.0254   # Spacing of the cut planes
    u = 1           # Inlet velocity (assumed uniform at inlet)
    Pr = 0.7        # Prandtl number of the fluid
    rho = 1.225     # Density of the fluid
    mu = 1.79e-5    # Dynamic viscosity of the fluid

    Re_D = rho*u*D/mu                       # Reynolds number
    data['h'] = data['q']/(data['Tm']-data['Tw'])   # Heat Transfer coefficient at each cut plane
    print(data['z'], data['h'])
    data['Nu_loc'] = data['h']*D/k          # Nusselt number at each cut plane
    #data['z'] = L - data['z']               # This was only needed for my case. I accidentaly put the inlet at x=L, instead


    # This is the trapezoidal integration to calculate the overall heat transfer coefficient
    h = 0                                   # Initialize the heat transfer coefficient
    for i in range(len(data['z'])-1):
        h += 1/L*dz/2*(data['h'].iloc[i+1]+data['h'].iloc[i])
    Nu_avg = np.abs(h*D/k)                  # Calculate average Nu, based on average (integrated) h
    print("Average Nusselt Number from ANSYS is",Nu_avg)

    """ # Commented out for dimpled analysis
    """
    # This is to calculate the analytical solution for Nu, if one exists.
    #x = np.linspace(0.001,0.1,100)          # x-direction matrix
    #beta_x = Re_D*Pr*D/x                    # Parameter used in next calculation
    #Nu_x = (49.371+(1.077*beta_x**(1/3)-0.7)**3+np.sqrt(0.03125/(1+22*Pr)*beta_x**3))**(1/3)

    # Plots for local Nusselt number
    plt.semilogy(data['z'],data['Nu_loc'])      # From ANSYS results
    print(data['Nu_loc'])
    #plt.semilogy(x,Nu_x,color="blue")           # Analytical solution (if one exists)
    #plt.ylim([0,25])
    plt.grid(True, which="both")
    plt.legend(['ANSYS Developing Flow'])#,'Analytical'])
    xticks = np.arange(0,0.2032,step=0.05)
    plt.xticks(xticks)
    plt.show()
```

Figure 76.—Python postprocessing script (Ref. 2).

Cell input	*0*	*1*	*2*	*3*	*4*	*5*	*6*	*7*	*8*	after reevaporation
Tg	295.7	284.7	282.6	281.8	281.1	280.4	279.7	279.1	278.4	277.5
Tc	283.0	282.3	281.6	281.0	280.3	279.6	278.9	278.3	277.6	
mv	9.85E-06	8.65E-06	8.19E-06	7.83E-06	7.50E-06	7.18E-06	6.87E-06	6.58E-06	6.29E-06	6.73E-06
mtot	2.0E-07	1.4E-06	1.9E-06	2.2E-06	2.5E-06	2.9E-06	3.18E-06	3.47E-06	3.76E-06	3.32E-06
Ti		283.5	282.4	281.7	281.0	280.3	279.7	279.0	278.3	
mcond		0	0	0	0	0	0	0	0	
qcondense		3.8E+02	1.5E+02	1.2E+02	1.1E+02	1.0E+02	9.8E+01	9.4E+01	9.1E+01	
qconv		1715	314	130	107	104	104	103	103	
qwall		2097	461	246	214	206	202	198	194	
mcell		0	0	0	0	0	0	0	0	
qcell		1.62E+01	3.56E+00	1.90E+00	1.65E+00	1.59E+00	1.56E+00	1.53E+00	1.50E+00	
hcell		379.2	363.0	359.4	357.5	355.8	354.2	352.7	351.1	
pcell		1297.8	1097.4	1031.8	983.2	939.0	896.9	856.5	817.7	
RHcell		47%	81%	87%	88%	88%	88%	88%	88%	
qcondense x A x layers		420	161	127	117	112	108	104	100	
qconv x A x layers		1883	345	143	118	114	114	114	113	
qcell x layers		2303	506	270	235	226	221	217	213	
mv x layers	0.00140	0.00123	0.00116	0.00111	0.00106	0.00102	0.00098	0.00093	0.00089	
mtot x layers	0.00003	0.00020	0.00026	0.00031	0.00036	0.00041	0.00045	0.00049	0.00053	
check energy conservation:		1.84E+02	6.20E+01	4.67E+01	4.25E+01	4.05E+01	3.88E+01	3.73E+01		

		cumulative, no revap	
W	**1248**	latent heat exchanged	
W	**2944**	sensible heat exchanged	
W	**4192**	total heat exchange	
kg/s	**5.33E-04**	total condensed vapor	
W	452.119	cumulative error	

Evaluate this block against the required performance

cumulative, with revap	
1164	latent heat exchanged
3028	sensible heat exchanged
4.71E-04	total condensed vapor
1030	

Figure 77.—Condensation and heat rate spreadsheet (Ref. 2).

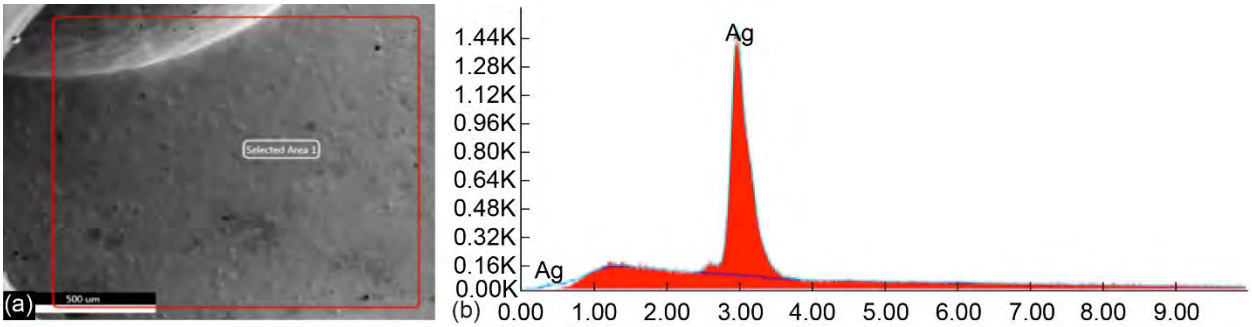

Figure 78.—EDAX positioning and results for processed sample at location 3 unprocessed region, position 6, 15 KeV. (a) SEM image of sample. (b) Spectroscopy analysis results; no iron detected.

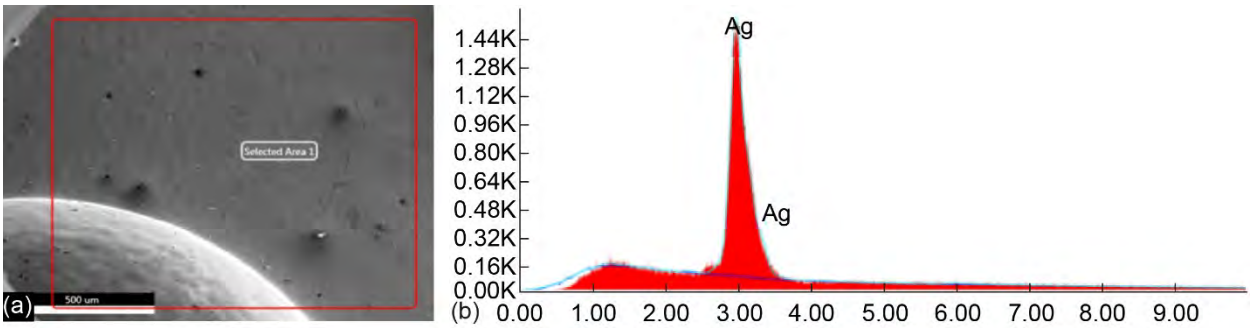

Figure 79.—EDAX positioning and results for processed sample at location 3 unprocessed region, position 7, 15 KeV. (a) SEM image of sample. (b) Spectroscopy analysis results; no iron detected.

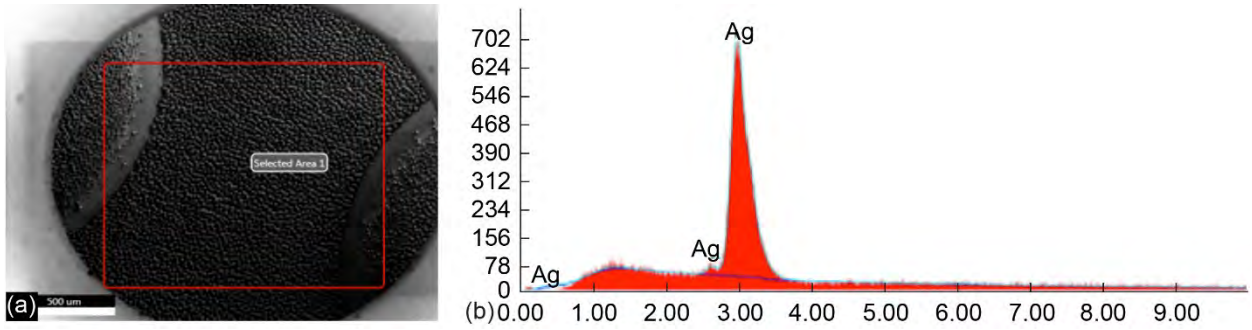

Figure 80.—EDAX positioning and results for processed sample at location 3 processed region, position 2, 15 KeV. (a) SEM image of sample. (b) Spectroscopy analysis results; no iron detected.

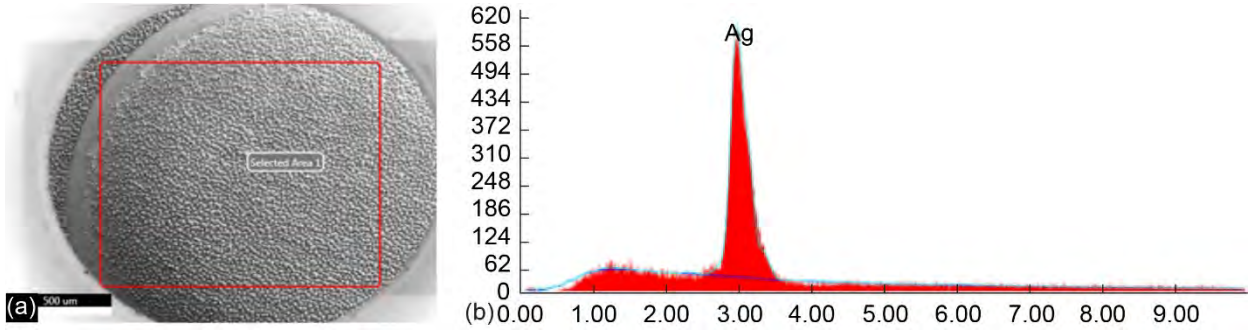

Figure 81.—EDAX positioning and results for processed sample at location 3 processed region, position 3, 15 KeV. (a) SEM image of sample. (b) Spectroscopy analysis results; no iron detected.

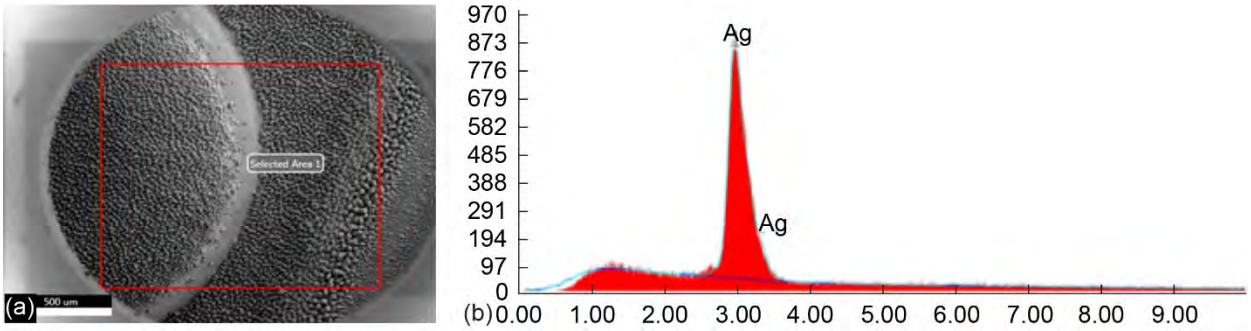

Figure 82.—EDAX positioning and results for processed sample at location 3 processed region, position 4, 15 KeV. (a) SEM image of sample. (b) Spectroscopy analysis results; no iron detected.

References

1. National Aeronautics and Space Administration: 2020 NASA Technology Taxonomy. 2020. https://www.nasa.gov/otps/2020-nasa-technology-taxonomy/ Accessed Nov. 11, 2023.
2. Monaghan, K.W., et al.: Polaris Project: Enabling Full Scale Laser Processed Condensing Heat Exchanger (LP-CHX) Manufacturing (LP-CHX). NASA Techport, 2022. https://techport.nasa.gov/projects/116430 Accessed March 3, 2022.
3. Hansen, Scott, et al.: Laser-Processed Condensing Heat Exchanger Technology Development. ICES-2018-72, 2018.
4. Hatch, Tyler R., et al.: Laser Processed Condensing Heat Exchanger for Space Applications. TFEC-2024-50521, 2024.
5. Roth, N., et al.: Creation of Micro/Nano Surface Structures on Silver Using Collinear Double Femtosecond Laser Pulses With Different Pulse Separation. Multiscale Multidiscip. Model. Exp. Des., vol. 1, 2018, pp. 145–153.
6. COMSOL: Which Turbulence Model Should I Choose for My CFD Application? 2017. https://www.comsol.com/blogs/which-turbulence-model-should-choose-cfd-application/ Accessed Nov. 11, 2023.
7. Ansys: Forced Convection Over a Flat Plate. 2021. https://courses.ansys.com/wp-content/uploads/2021/02/LT4_C2_L3-Handout-v2.pdf Accessed Nov. 12, 2023.
8. University of Nebraska-Lincoln College of Engineering: About. 2025. About | Center for Electro-Optics and Functionalized Surfaces (CEFS) | Nebraska Accessed April 3, 2025.
9. Zuhlke, C., et al.: Enabling Full-Scale Laser Processed Condensing Heat Exchanger (LP-CHX) Manufacturing. University of Nebraska-Lincoln Presentation, 2023. Available from the NASA STI Program.
10. ATSM B700-20: Standard Specification for Electrodeposited Coatings of Silver for Engineering Use. ASTM International, West Conshohocken, PA, 2020.
11. ATSM B571-23: Standard Practice for Qualitative Adhesion Testing of Metallic Coatings. ASTM International, West Conshohocken, PA, 2023.
12. Mena, C.; and Wallace, S.: Enabling Full Scale Laser Processed Condensing Heat Exchanger (LP-CHX) Manufacturing: Microbial Evaluation. JSC Microbiology Laboratory. Available from the NASA STI Program.
13. Hansen, Scott, et al.: Laser Processed Condensing Heat Exchanger Technology Development. ICES-2017-295, 2017.
14. Hansen, Scott, et al.: Laser Processed Condensing Heat Exchanger (LP-CHX) Test Article Design, Manufacturing, and Testing. ICES-2021-60, 2021.